10-2023

Snowpack Relative Permittivity and Density Derived from Near-Coincident Lidar and Ground-Penetrating Radar

Randall Bonnell
Colorado State University

Daniel McGrath
Colorado State University

Andrew R. Hedrick
USDA Agricultural Research Service

Ernesto Trujillo
Boise State University

Tate G. Meehan
U.S. Army Corps of Engineers

See next page for additional authors

Authors

Randall Bonnell, Daniel McGrath, Andrew R. Hedrick, Ernesto Trujillo, Tate G. Meehan, Keith Williams, Hans-Peter Marshall, Graham Sexstone, John Fulton, Michael J. Ronayne, Steven R. Fassnacht, Ryan Webb, and Katherine E. Hale

WILEY

Snowpack relative permittivity and density derived from near-coincident lidar and ground-penetrating radar

Randall Bonnell[1] | Daniel McGrath[1] | Andrew R. Hedrick[2] |
Ernesto Trujillo[2,3] | Tate G. Meehan[4] | Keith Williams[5] | Hans-Peter Marshall[3] |
Graham Sexstone[6] | John Fulton[6] | Michael J. Ronayne[1] |
Steven R. Fassnacht[7,8] | Ryan W. Webb[9] | Katherine E. Hale[10]

[1]Department of Geosciences, Colorado State University, Fort Collins, Colorado, USA

[2]Northwest Watershed Research Center, USDA Agricultural Research Service, Boise, Idaho, USA

[3]Department of Geosciences, Boise State University, Boise, Idaho, USA

[4]Cold Regions Research and Engineering Laboratory, U.S. Army Corps of Engineers, Hanover, New Hampshire, USA

[5]GAGE Facility, UNAVCO Inc., Boulder, Colorado, USA

[6]U.S. Geological Survey, Colorado Water Science Center, Denver, Colorado, USA

[7]ESS-Watershed Science, Colorado State University, Fort Collins, Colorado, USA

[8]Cooperative Institute for Research in the Atmosphere, Colorado State University, Fort Collins, Colorado, USA

[9]Department of Civil and Architectural Engineering and Construction Management, University of Wyoming, Laramie, Wyoming, USA

[10]Department of Civil and Environmental Engineering, University of Vermont, Burlington, Vermont, USA

Correspondence
Randall Bonnell, Department of Geosciences, Colorado State University, Fort Collins, CO, USA.
Email: randall.bonnell@colostate.edu

Abstract

Depth-based and radar-based remote sensing methods (e.g., lidar, synthetic aperture radar) are promising approaches for remotely measuring snow water equivalent (SWE) at high spatial resolution. These approaches require snow density estimates, obtained from in-situ measurements or density models, to calculate SWE. However, in-situ measurements are operationally limited, and few density models have seen extensive evaluation. Here, we combine near-coincident, lidar-measured snow depths with ground-penetrating radar (GPR) two-way travel times (*twt*) of snowpack thickness to derive >20 km of relative permittivity estimates from nine dry and two wet snow surveys at Grand Mesa, Cameron Pass, and Ranch Creek, Colorado. We tested three equations for converting dry snow relative permittivity to snow density and found the Kovacs et al. (1995) equation to yield the best comparison with in-situ measurements (RMSE = 54 kg m^{-3}). Variogram analyses revealed a 19 m median correlation length for relative permittivity and snow density in dry snow, which increased to >30 m in wet conditions. We compared derived densities with estimated densities from several empirical models, the Snow Data Assimilation System (SNODAS), and the physically based iSnobal model. Estimated and derived densities were combined with snow depths and *twt* to evaluate density model performance within SWE remote sensing methods. The Jonas et al. (2009) empirical model yielded the most accurate SWE from lidar snow depths (RMSE = 51 mm), whereas SNODAS yielded the most accurate SWE from GPR *twt* (RMSE = 41 mm). Densities from both models generated SWE estimates within ±10% of derived SWE when SWE averaged >400 mm, however, model uncertainty increased to >20% when SWE averaged <300 mm. The development and refinement of density models, particularly in lower SWE conditions, is a high priority to fully realize the potential of SWE remote sensing methods.

KEYWORDS
ground-penetrating radar, lidar, remote sensing, snow density, snow modeling, snow water equivalent

1 | INTRODUCTION

Seasonal snow covers up to 60% of the Northern Hemisphere land area (Hammond et al., 2018; Kim, 2018) and serves as a vital water resource for ecosystems spanning prairies, mountains, tundra, and boreal forests (Sturm et al., 1995). Mountains tend to accumulate deep snowpacks that provide water resources for one sixth of the world's population (Barnett et al., 2005; Mankin et al., 2015). In North America, mountains comprise 25% of the land area but store 60% of the total snow water equivalent (SWE; Wrzesien et al., 2018). Warming in the mountainous western United States (U.S.) has caused SWE losses of 15%–30% over the last 70 years (Mote et al., 2018), while a further 25% loss in SWE is predicted by 2050 (Siirila-Woodburn et al., 2021). These changes, compounded with human dependence upon snow water resources, make the pursuit of global SWE estimates a highly prioritized, trillion-dollar endeavour (National Academies of Sciences, Engineering, and Medicine, 2018; Sturm, 2015). Currently, no single method or ensemble of methods has proven capable of measuring SWE to the high standard of accuracy established for global monitoring (Dozier et al., 2016). Recent campaigns, such as the U.S.-based National Aeronautics and Space Agency (NASA) Snow Experiment (SnowEx; Durand et al., 2018) and the Europe-based NoSREx and APRESS (Tsang et al., 2022), evaluated a suite of remote sensing approaches (e.g., lidar, radar) for SWE-mapping applications. At the watershed scale, light detection and ranging (lidar) operations, such as the Airborne Snow Observatory (ASO), have demonstrated operational feasibility (Deems et al., 2013; Painter et al., 2016), but can be cost prohibitive. Satellite remote sensing methods for SWE-mapping have been under development for decades (Dietz et al., 2012; Nolin, 2010; Shi et al., 2016) and see continued interest, particularly in data assimilation applications, wherein derived snow products are integrated within physically based snow models (Largeron et al., 2020). For simplification, we discuss two major approaches of snow remote sensing: depth-based and radar-based methods. Both approaches have high spatial resolution and accuracy and are thus forerunners in the development of satellite-based SWE retrievals in mountains (Dozier et al., 2016).

Measuring SWE from depth-based remote sensing approaches relies on differencing repeat surface elevation measurements (i.e., snow-free from snow-on elevation surfaces) to derive snow depth (Currier et al., 2019; Deems et al., 2013). For this approach, SWE is the product of the derived snow depth (d_s) and snow density (ρ_s):

$$SWE_{depth-based} = d_s \times \rho_s. \tag{1}$$

Depth-based methods are primarily limited to the optical to near infrared portion of the electromagnetic spectrum, where atmospheric transmission is high, and wavelengths are significantly smaller than snow grains. Depth-based methods, including photogrammetry and lidar, have demonstrated potential for satellite platforms (Enderlin et al., 2022; Shean et al., 2016).

Radar-based methods further require an estimate of relative permittivity (ε_s) to characterize the electromagnetic wave velocity of the snowpack to derive snow depth, and thereby SWE, from the signal path length (l_p; e.g., two-way travel time; Marshall et al., 2005). Thus, radar-based SWE is generally expressed as a function,

$$SWE_{radar-based} = f(l_p, \varepsilon_s(\rho_s, \theta_{LWC})), \tag{2}$$

where the relative permittivity, a measure of the ability of a material to store charge relative to free-space (Daniels, 2004), is controlled by the snow density and volumetric liquid water content (LWC; θ_{LWC}). In dry snow, dielectric permittivity is primarily determined by snow density. However, wet snow permittivity exhibits a large dependence on LWC because the relative permittivity of water is ∼60 times that of snow (Bonnell et al., 2021). LWC induces the imaginary component of relative permittivity and acts as a frequency-dependent attenuator of signal strength (Koch et al., 2014), an attribute which was leveraged by Bradford et al. (2009) as the first study to derive spatially distributed LWC along a ground-penetrating radar (GPR) transect. At least six equations have been published for the relative permittivity of wet snow, whereas there are >19 published equations relating the relative permittivity of dry snow to its density, effectively increasing the uncertainty of radar-based SWE retrievals due to a large range in permittivity for a given snow density (Di Paolo et al., 2020). Not all radar SWE retrieval approaches utilize the signal path length through the snow. Some approaches, such as the Ka-band interferometry for wet snow conditions (Moller et al., 2017), may be better described as depth-based approaches, whereas Synthetic Aperture Radar (SAR) backscatter approaches rely on empirical models that are at least partly dependent on the snowpack relative permittivity (Tsang et al., 2022).

Density, a required input for both SWE approaches, can be either modelled or measured in snow pits, along snow courses, or by automated weather stations with a depth sensor co-located above a snow pillow. Density varies at the hillslope scale (Alford, 1967) due to differences in overburden pressure, radiation inputs, and wind and precipitation patterns (Winkler et al., 2021). However, density tends to vary less than snow depth, and because manual measurements are time-consuming, studies generally assume limited spatial snow density variability (López-Moreno et al., 2013; Shook & Gray, 1996; Sturm et al., 2010). Thus, current density sampling approaches may acquire measurements too sparsely to capture its inherent spatial variability (Meehan, 2022), making snow density models an appealing alternative for remote sensing approaches.

Selecting an appropriate density model can be difficult. There are three broad categories: empirical models (Avanzi & De Michele, 2015), physically based models (e.g., Havens et al., 2020; Lehning, Bartelt, Brown, & Fierz, 2002; Lehning, Bartelt, Brown, Fierz, & Satyawali, 2002; Marks et al., 1999), and data assimilation systems (Largeron et al., 2020), and within each category, numerous models exist. Additionally, validation efforts outside of the original publications are limited. Empirical models are developed using a statistical relation between snow density, a time parameter (e.g., month),

and, in more complicated equations, snow depth and geographic metrics. Physically based models can be powerful predictive tools but tend to be computationally expensive, require extensive meteorological forcing datasets, and often use simplified densification formulas (Hedrick et al., 2018). Empirical models can be simpler to implement and produce statistically robust estimates at the interannual scale, however few accurately capture short-term variability in snow density (McCreight & Small, 2014). Empirical models requiring snow depth as an input cannot be directly inserted into radar SWE retrieval equations because radar methods cannot estimate depth independently from density. Some of these models have been intercompared to assess sensitivity and bias (e.g., Avanzi & De Michele, 2015; McCreight & Small, 2014; Raleigh & Small, 2017), but comparisons have been limited by the scope of available in-situ snow density measurements. Density estimates from data assimilation methods are a third option, though measurements are coarse in resolution (>1 km; Largeron et al., 2020). Recently published density models include a semi-empirical model that balances computational efficiency by implementing a simplified physically based snow compaction equation within an empirical framework (Winkler et al., 2021), and empirical models that estimate snow density from a suite of lidar-derived parameters (Bisset et al., 2022; Meehan, 2022). Both model types are optimized for depth-based remote sensing methods: the semi-empirical model ingests repeat-measured snow depths acquired with low temporal baselines (≤7 days) and may be implemented for any given year/location, whereas lidar-derived models are designed and implemented for a single lidar survey (Meehan, 2022).

GPR measures the two-way travel time (*twt*) of the radar wave through the snowpack, which can be combined with lidar-measured snow depths to estimate radar velocity and relative permittivity. Several studies have established this method and converted relative permittivity to LWC by constraining snow density using snow pit measurements (Bonnell et al., 2021; Heilig et al., 2015; Webb et al., 2018; Webb, Wigmore, et al., 2020). More recent studies have used this technique to derive snow density by coupling uncrewed aerial vehicle (UAV) Structure from Motion (SfM) measurements of snow depth with GPR-measured *twt* and identified spatial variabilities that were larger than variabilities mapped by previous in-situ studies (McGrath et al., 2022; Yildiz et al., 2021). We expanded on previous work by leveraging a time series of GPR and lidar datasets from Grand Mesa and Cameron Pass, Colorado, and a one-off survey conducted at Ranch Creek, Colorado. We combined lidar-measured snow depths with GPR-measured *twt* of the snowpack thickness to derive spatially distributed relative permittivity in both dry and wet conditions. For dry-snow surveys only, relative permittivity is converted to density using three different equations to illustrate the variability in published equations. We then compared the derived densities with in-situ measurements and selected the most representative equation. Given the upcoming launches of L-band (1–2 GHz) SAR satellites (e.g., ALOS-4, NISAR, ROSE-L, and TanDEM-L) and their potential for global SWE-monitoring (Deeb et al., 2011; Guneriussen et al., 2001; Marshall et al., 2021; Tarricone et al., 2023), we estimated the spatial variability of derived relative permittivity and snow density at the approximate

scale of SAR satellite platforms by conducting a variogram analysis. Derived densities were then used to evaluate modelled densities from four empirical models, the Snow Data Assimilation System (SNODAS; Barrett, 2003), and iSnobal (Lehning, Bartelt, Brown, & Fierz, 2002; Lehning, Bartelt, Brown, Fierz, & Satyawali, 2002), with particular attention given to model performance within depth-based and radar-based SWE remote sensing methods.

2 | FIELD SITES

We used 1.0 and 1.6 GHz centre-frequency (L-band) GPR *twt* measurements of the snowpack thickness, lidar-measured snow depths, and snow pit-measured densities collected during the NASA SnowEx 2017 Grand Mesa Campaign, the NASA SnowEx 2020–21 Time Series Campaigns at Cameron Pass, and a single survey led by the U.S. Geological Survey (USGS) at Ranch Creek in 2021 (Figure 1). An overview of the dates and technical aspects of the instrumentation used at each field site is shown in Table 1.

SnowEx 2017 was conducted from 6 to 25 February of water year (WY) 2017 at Grand Mesa (Figure 1f,g). The campaign consisted of three (8, 16, and 25 February) airborne lidar surveys, collected and processed by ASO (Painter, 2018). Surface-coupled, common-offset GPR (Webb et al., 2019) was collected daily on a sled pulled behind either a skier/snowshoer or snowmobile along transects and small grids. Two adjacent SNOTEL stations, Park Reservoir and Mesa Lakes SNOTELs, recorded negligible net changes in snow depth (+0.00–0.03 m) for 8–16 February and modest net increases (+0.03–0.08 m) for 16–25 February (Figure S1a,d). For the 8 and 16 February flights, we selected only GPR collected ±2 days around the ASO flight date to limit the uncertainty of snow deposition that occurred on 11–12 February, resulting in 4.8 km of GPR data for the 8 February flight and 8.8 km for the 16 February flight. GPR efforts during the third week of the campaign were focused on small-scale (<500 m) variability. Because limited snow accumulation (<5 mm SWE) occurred after 20 February, the 2.6 km of GPR collected from 21 to 25 February were included.

The Cameron Pass and Ranch Creek field sites (Figure 1b–e; <0.5 km^2) are much smaller than Grand Mesa (46 km^2). However, Cameron Pass was one of several sites observed during the NASA SnowEx 2020–21 Time Series Campaigns (Marshall et al., 2019) and thus offers a longer time series that spans two accumulation seasons and one ablation season. Ranch Creek was also surveyed during the ablation season and adds information to the distribution of relative permittivity in wet snowpacks. At Cameron Pass, terrestrial lidar scans (TLS) were collected on 18 December, 26 February, and 12 March during WY 2020 and on 10, 24 February, 22 March, and 27 May during WY 2021 (Williams, 2021). This site included repeat 0.5 km GPR transects in 2020 and repeat 0.9 km transects in 2021 (Bonnell et al., 2022; McGrath et al., 2021). The nearby Joe Wright SNOTEL station (Figure S1b,e) recorded snow depth changes of +0.97 m (+280 mm SWE) and −0.17 m (+40 mm SWE) between the three WY 2020 surveys, and +0.10 m (+59 mm SWE), +0.41 m (+119 mm
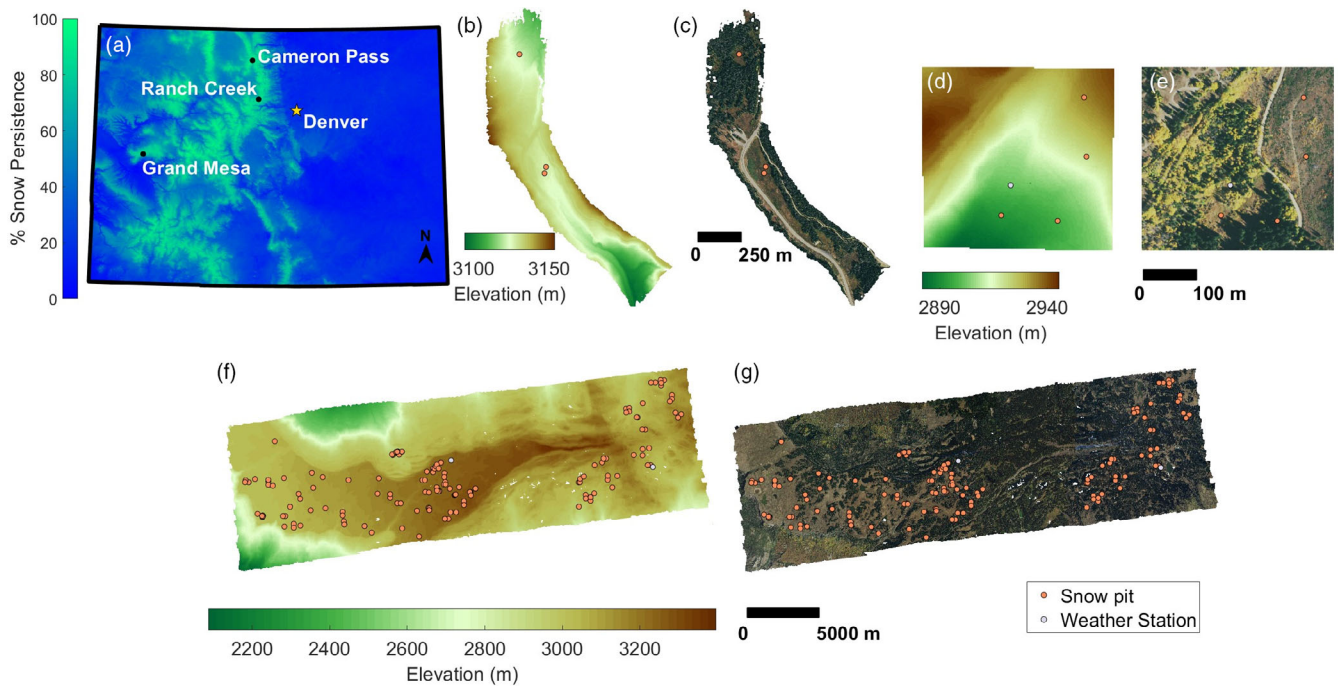
FIGURE 1 (a) Location of field sites within Colorado and 1 January to 1 July snow persistence (Moore et al., 2015). (b) Digital elevation model (DEM) and (c) National Agricultural Imagery Program (NAIP imagery of Cameron Pass, with snow pit locations. (d) DEM (Bauer et al., 2023) and (e) NAIP imagery of Ranch Creek, with weather station and snow pit locations. (f) DEM (Painter & Bormann, 2020) and NAIP imagery of Grand Mesa, with locations of SNOTEL stations and snow pits. Figure scales and colour ramps differ by field site. The vertical datums are the WGS84 Ellipsoid for Grand Mesa and the NAVD88 Geoid 18 for Cameron Pass and Ranch Creek. NAIP imagery acquired from USGS Earth Explorer (https://earthexplorer.usgs.gov/, accessed 10 October 2022).

TABLE 1 Technical details of the instrumentation and datasets for each of the field sites in Colorado.

Study site	Grand Mesa	Cameron Pass	Ranch Creek
Date range	*WY 2017*: 8–25 February	*WY 2020*: 18 December–12 March *WY 2021*: 10 February–27 May	*WY 2021*: 7 April
Lidar platform	Airborne Riegl Q1560	Terrestrial Riegl VZ-2000/6000 UAV Yellowscan VX20	UAV Yellowscan VX20
GPR system	MALA ProEx 1.6 GHz	Sensors & Software PulseEkko 1.0 GHz	Sensors & Software PulseEkko 1.0 GHz
Study site area	500 km^2	0.10 km^2	0.10 km^2
Data boundaries	*Latitude*: 38.941, 39.152 *Longitude*: −108.259, −107.820	*Latitude*: 40.512, 40.527 *Longitude*: −105.896, −105.884	*Latitude*: 39.912, 39.916 *Longitude*: −105.763, −105.757
Coordinate systems	*Horizontal*: WGS84/UTM Zone 13N *Vertical*: WGS84 Ellipsoid	*Horizontal*: NAD83 (2011)/UTM Zone 13N *Vertical*: NAVD88/GEOID18	*Horizontal*: NAD83 (2011)/UTM Zone 13N *Vertical*: NAVD88/GEOID18
Vegetation summary	*Open*: Grasses and Shrubs *Forest*: Lodgepole, Spruce, Fir, Aspen	*Open*: Mixed Willows and Grasses	*Open*: Mixed Willows *Forest*: Lodgepole and Aspen

Note: Water Year is abbreviated to WY. Grand Mesa vegetation summary sourced from Webb, Raleigh, et al. (2020). Cameron Pass and Ranch Creek vegetation notes were taken in the field and verified with Huckaby and Moir (1998) and Fassnacht et al. (2018).

SWE), and −0.84 m (−104 mm SWE) between the four surveys conducted in WY 2021. Ranch Creek was surveyed on 7 April 2021 using a lidar system borne by a UAV (Bauer et al., 2023), while 2.9 km of GPR data were collected in a spiral survey design (Bonnell &

McGrath, 2023). The Ranch Creek survey was conducted 10 days after peak SWE was observed by the nearby USGS weather station (29 March; Figure S1c,f), which had lost 0.31 m snow depth (135 mm SWE) over that same time period.

3 | METHODS

3.1 | Calculating relative permittivity and snow density

Lidar-measured snow depths were collected from one of three platforms: airborne (Grand Mesa), terrestrial (Cameron Pass), and UAV-borne (Ranch Creek). GPR radargrams were collected as common-offset surveys via a sled coupled to the snow surface and utilized L-band centre-frequency. Processing of lidar point clouds collected by terrestrial and UAV platforms generally followed the workflow outlined by Currier et al. (2019), whereas radargram processing and picking of snowpack *twt* thickness followed McGrath et al. (2019). Appendix A.1 provides further details of the data processing.

A common practice of GPR in snow applications is to convert the *twt* of the snowpack thickness to snow depth (d_s; e.g., Lundberg et al., 2006; Marshall et al., 2005), using an estimate of the snowpack radar velocity (v_s; Daniels, 2004):

$$d_s = \frac{twt}{2} \times v_s. \tag{3}$$

Radar velocity is estimated from the relative permittivity of the snowpack,

$$v_s = \frac{c}{\sqrt{\varepsilon_s}}, \tag{4}$$

where, c is the velocity of electromagnetic radiation in a vacuum. Here, we constrain the snow depth using lidar and directly estimate relative permittivity:

$$\varepsilon_s = \left(\frac{c \times twt}{2d_s}\right)^2. \tag{5}$$

In dry snow, snow density can be estimated directly from a relative permittivity equation. Because the choice of an equation is not straightforward (Di Paolo et al., 2020), we calculated snow density from three permittivity equations. Of the published equations and for a given relative permittivity, the Kovacs et al. (1995) equation (Equation 6) estimates the median density, the Kuroiwa (1954) equation (Equation 7) estimates the minimum density, and the Webb et al. (2021) equation (Equation 8) estimates the maximum density (Di Paolo et al., 2020). The three equations are:

$$\varepsilon_s = \left(1 + 0.845\frac{\rho_s}{1000}\right)^2, \tag{6}$$

$$\varepsilon_s = 1 + 2.3\frac{\rho_s}{1000}, \tag{7}$$

$$\varepsilon_s = 1 + 1.4 \times 10^{-3}\rho_s + 2 \times 10^{-7}\rho_s{}^2. \tag{8}$$

The equations are written such that units for density (ρ_s; kg m^{-3}) are consistent.

Measurements of *twt* were binned within lidar grid cells (3 m × 3 m) by calculating the median *twt* value per cell. Grid cells that did not meet a minimum threshold of 15 *twt* measurements within the cell were removed from the analysis. Relative permittivity was calculated from coincident snow depth and *twt* cells (Equation 5). Previous studies have established a large randomly distributed error in the relative permittivity estimates that results from uncertainties in snow depths and *twt*, but with sufficient sampling and filtering, a robust estimate can be established (Bonnell et al., 2021; McGrath et al., 2022; Meehan, 2022). Erroneous relative permittivity values (e.g., $\varepsilon_s < 1$) were reduced by removing all values outside of the inter-quartile range. Uncertainties were further reduced by smoothing the remaining relative permittivity estimates with a 21 m × 21 m moving window median filter. A filter of this size was chosen to retain spatial variability along the transect-oriented surveys. We categorized surveys as dry or wet based on the presence of any LWC noted in snow pits and corroborated by pit temperatures (Appendix A.2; Figure S2). Relative permittivity estimates obtained in dry-snow conditions (all surveys, except the 7 April and 27 May 2021 surveys) were then converted to density using the Kovacs et al. (1995), Kuroiwa (1954), and Webb et al. (2021) equations and compared to in-situ density measurements to calculate the RMSE and Pearson correlation coefficient to determine the most representative equation.

3.2 | Uncertainty analysis

We estimated the uncertainty in relative permittivities through Monte Carlo simulations for each survey date. The mean snow depth and *twt* were calculated from the 3 m rasters. Grand Mesa lidar snow depth uncertainty was estimated from the extensive comparisons between the Grand Mesa airborne lidar and snow depth probes established by Currier et al. (2019). For Cameron Pass, the lidar snow depth uncertainty was estimated using the standard deviation of elevational differences between the bare-earth and snow-on DEMs along the CO-14 highway surface. The Ranch Creek lidar snow depth uncertainty was estimated from comparison with surveyed ground control points (Bauer et al., 2023). Uncertainties in *twt* were estimated from the mean within-pixel *twt* standard deviation for each survey date. Then, Monte Carlo simulations with 100 000 realizations from Equations (4) and (5) were performed using a random normal distribution, where the uncertainty estimates were considered representative of the standard deviation around the mean snow depth and *twt*. This established estimates for the mean and standard deviations of derived relative permittivity and snow density for each survey date, which is estimated as the uncertainty range in our derived relative permittivity and snow density datasets. All Monte Carlo simulation parameters and estimates are listed in Table S1.

3.3 | Variogram analysis

We conducted a variogram analysis using a lag spacing of 10 m, which approximates the spatial resolution of SAR satellites. Variance at the lag spacing, γ(h), for experimental variograms is given as,

$$\gamma(h) = \left(\frac{1}{2N(h)}\right) * \sum_{i=1}^{N(h)} (x_i - x_{i+h})^2, \quad (9)$$

where, $N(h)$ is the number of point-pairs at the given lag spacing and x is the variable of interest (Anderson et al., 2014; Schwanghart, 2022a; Webster & Oliver, 2001). Omni-directional experimental variograms were computed from the datasets for snow depth, twt, relative permittivity, snow density, and SWE (achieved by multiplying the derived snow density by its corresponding snow depth). Experimental variograms were computed using the same grid cells across all variables for the given survey date. Based on the shape of calculated experimental variograms, we identified the exponential model as the most representative variogram model for each of the variables. The exponential variogram model with a nugget effect is given as

$$\gamma(h) = s_0 + s * \left(1 - e^{-\frac{h}{a}}\right), \quad (10)$$

where, a is the correlation distance, s_0 is the nugget effect, and s is the exponential model contribution to the sill (Isaaks & Srivastava, 1989). Variogram model parameters were estimated by least-squares fitting (Schwanghart, 2022b). For the Grand Mesa datasets, sufficient GPR observations were collected in forests to enable variogram analyses of snowpacks in both forests and open environments. Following McGrath et al. (2019), we chose a 2 m vegetation height metric and used the ASO vegetation heights dataset collected in Fall 2016 (Painter & Bormann, 2020) to generate a binary forest/open mask. Variograms were not calculated for snow density or SWE when LWC was present in the snowpack (i.e., 7 April and 27 May 2021).

3.4 | Modeling snow density

We tested density estimates from four empirical models, SNODAS, and iSnobal against our derived density dataset. Evaluated empirical models include Mizukami and Perica (2008; M&P_08), Jonas et al. (2009; J_09), Sturm et al. (2010; St_10), and Sexstone and Fassnacht (2014; S&F_14). Of these, St_10 and J_09 have global applications and were previously implemented in a lidar SWE-retrieval study (Raleigh & Small, 2017). We included S&F_14, developed for the watershed adjacent to Cameron Pass, to evaluate whether a locally derived model offers any advantage over global models. M&P_08 is a simpler model, designed to ingest only the day-of-year (DOY) and a snow climate parameter, but Pistocchi (2016) suggests such models can be statistically robust, and it is one of the few empirical models which can be ingested into a radar-based remote sensing method. SNODAS was chosen to represent data assimilation methods, given its use as a benchmark for evaluating larger scaled models (Broxton et al., 2016) and history of validation efforts (Clow et al., 2012; Hedrick et al., 2015; Lv et al., 2019). The iSnobal model (Havens et al., 2020; Marks et al., 1999) was chosen because of its incorporation into lidar SWE products geared toward operational water supply applications

(Painter et al., 2016). iSnobal was run over Cameron Pass for both unscaled (iSn_un) and rescaled (iSn_re; e.g., Hale et al., 2023; Kiewiet et al., 2022; Voegeli et al., 2016) precipitation scenarios because the chosen atmospheric model used for meteorological forcing within iSnobal, the High Resolution Rapid Refresh (HRRR) model, has been shown to underreport SWE by up to 25% (Meyer et al., 2023). Only surveys with dry snow conditions were modelled. An overview of the model parameters is given in Table S2 and further details regarding model runs are provided in Appendix A.3.

All modelled densities were compared with derived densities and the average of the in-situ measurements. Modelled densities were incorporated with lidar snow depths and GPR twt to calculate depth-based SWE and radar-based SWE. In-situ measurements were averaged for each date and used to calculate depth-based SWE from the lidar snow depths and radar-based SWE from twt to evaluate the efficacy of snow models compared to the 'gold standard'. The RMSE was then calculated for modelled versus derived densities, modelled and in-situ versus derived depth-based SWE, and modelled and in-situ versus derived radar-based SWE.

4 | RESULTS

4.1 | Overview of the derived relative permittivity and snow density datasets

We evaluated the lidar-GPR derived snow densities from the three relative permittivity equations using 40 snow pits from Grand Mesa (median = 322 kg m^{-3}, range = 93 kg m^{-3}) and six snow pits from Cameron Pass (median = 255 kg m^{-3}, range = 92 kg m^{-3}). Ranch Creek was excluded from this analysis because of wet snow conditions. Grand Mesa snow pits had an average of 19 derived snow densities within 30 m of each pit, whereas Cameron Pass averaged 11. When compared to snow pit measurements, the Kovacs et al. (1995), Kuroiwa (1954), and Webb et al. (2021) derived densities yielded overall RMSEs of 54 kg m^{-3} ($r = 0.09$), 97 kg m^{-3} ($r = 0.07$), and 83 kg m^{-3} ($r = 0.08$), respectively (Figure 2; Table S3). Both the Kovacs et al. (1995) and Kuroiwa (1954) equations yielded densities with an overall negative bias, whereas the Webb et al. (2021) equation yielded densities with a positive bias (Table S3). However, the mean residual for the Kuroiwa (1954) derived densities was three times the mean residual of the Kovacs et al. (1995) derived densities. At Cameron Pass, the Kuroiwa (1954) RMSE was 25% lower than Kovacs et al. (1995; Table S3), but frequently yielded physically unrealistic snow densities (e.g., <50 kg m^{-3} on 10 February 2021). Therefore, we selected the Kovacs et al. (1995) equation to use at both Grand Mesa and Cameron Pass because of its overall lower RMSE and more physically realistic snow densities.

We established survey-dependent uncertainty ranges for the derived relative permittivity and snow density datasets (Table S1) and found that the uncertainties in derived relative permittivity are more sensitive to snow depth than twt. At lower mean snow depths (<1 m), the effect of the snow depth uncertainty is increased, and large

FIGURE 2 (a) Relative permittivity equations from Kuroiwa (1954), Kovacs et al. (1995), and Webb et al. (2021). (b) Median derived snow density (considering all values within 30 m of the snow pit) versus measured snow density. Snow densities were derived using the three relations (Equations 6–8) presented in panel (a).
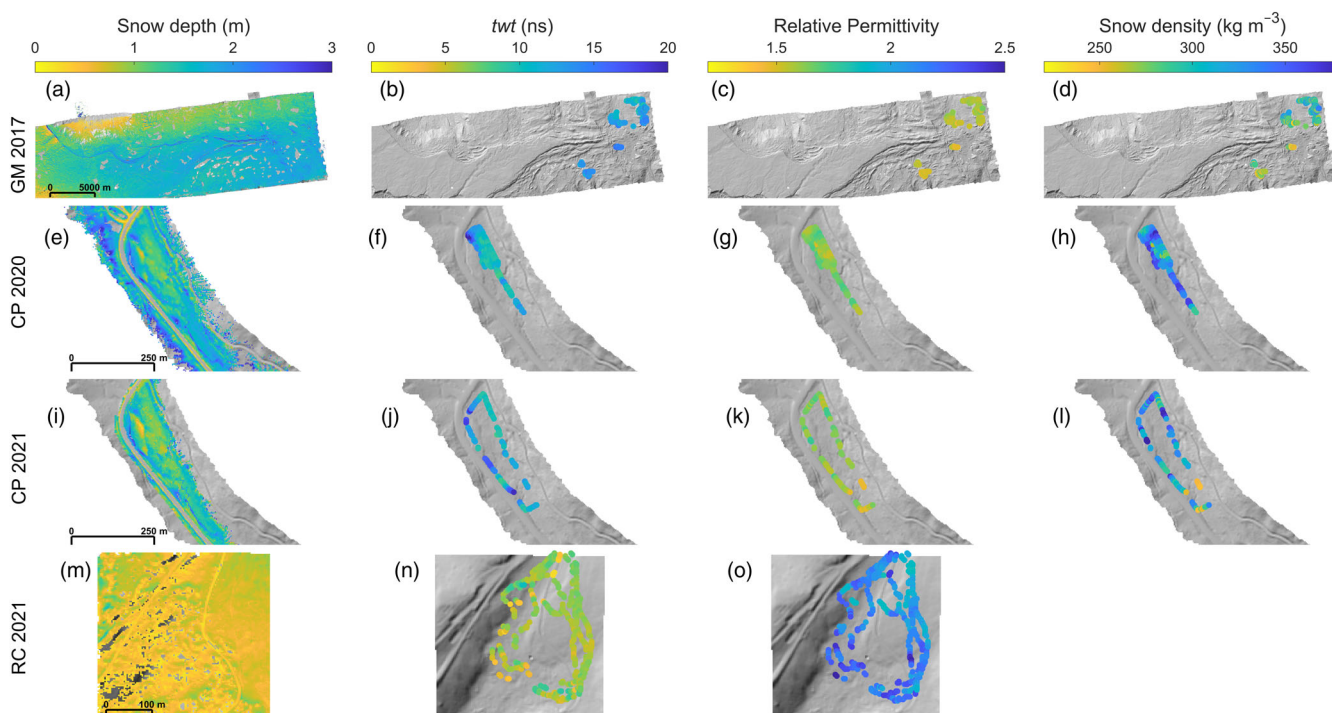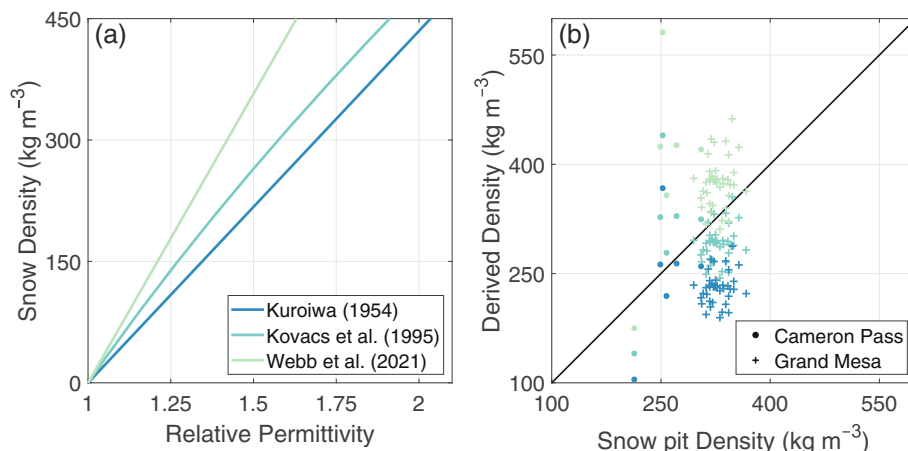
FIGURE 3 Examples from each field site and study year of the datasets used in this study. Rows are organized by field site, with (a–d) the 16 February 2017 Grand Mesa survey (GM 2017), (e–h) the 12 March 2020 Cameron Pass survey (CP 2020), (i–l) the 22 March 2021 Cameron Pass survey (CP 2021), and (m–o) the 7 April 2021 Ranch Creek survey (RC 2021). Columns are organized from left to right as snow depth, *twt*, relative permittivity, and snow density.

relative permittivity uncertainties result, leading to unrealistic estimates (e.g., $\varepsilon_s < 1$ and $\varepsilon_s > 88$). The average uncertainty for densities derived from TLS (196 kg m^{-3}) is approximately twice the average for those derived from airborne lidar (88 kg m^{-3}). This is primarily due to the lower average snow depths observed at Cameron Pass and the larger snow depth uncertainty range for the TLS platform. Differences between GPR systems did not have a substantial effect on estimated *twt* uncertainty, likely because of the similar vertical resolutions (calculated as one fourth of the wavelength; Daniels, 2004) of the 1.6 GHz (∼0.04 m) and 1.0 GHz (∼0.06 m) systems.

A subset of lidar snow depths, *twt*, derived relative permittivities, and derived snow densities are shown for Grand Mesa, Cameron Pass, and Ranch Creek in Figure 3. Although the full spatial extent of lidar and *twt* datasets are displayed, only snow depths that were used to derive relative permittivity values are discussed. All snow depth, *twt*, derived relative permittivity, and derived density datasets are plotted in Figures S3–S6. Results for Cameron Pass 2020 and 2021 are discussed as a time series. Although the Grand Mesa lidar was collected in sequential dates, Grand Mesa results are not treated as a time series because each week had a different region of interest for GPR

surveys. An overview of the mean and standard deviations for each of the datasets can be found in Table S4.

The lowest mean snow depth/*twt* at Grand Mesa was observed on forested transects on 8 February (1.19 m, 9.90 ns; Table S4), whereas the largest mean depth/*twt* was observed on open transects on 25 February (1.65 m, 13.55 ns). Forests exhibited lower mean snow depths and *twt* (−0.16 m, −1.37 ns) compared with open environments, resulting in a negligible, but consistently lower average snow density (mean difference = −5 kg m^{-3}) in forested environments. Although this contrast is within the uncertainty range of our method, two-sample *t*-tests suggest a statistically significant difference between the mean snow densities in forests and open environments during 16 and 25 February ($p < 0.005$). Further, snow pit-measured bulk densities ($n = 193$; Elder et al., 2018) corroborate the contrast but reveal a somewhat lower average snow density for forests (mean difference = −11 kg m^{-3}). Forested and open relative permittivity and density standard deviations showed negligible differences for each survey date (±0.006, ±3 kg m^{-3}).

Mean snow depths at Cameron Pass for WY 2020 increased from 0.66 to 1.34 m, while mean *twt* increased from 5.42 to 11.39 ns (Table S4). The mean snow depth did not change between 26 February and 12 March, however, the mean derived relative permittivity increased from 1.539 to 1.632, corresponding to an increase in density from 284 to 328 kg m^{-3}. As snow depths and SWE increased, standard deviations for derived relative permittivity and snow density decreased, relative to the 18 December 2019 survey, by 37% for the 26 February 2020 survey and by 56% for the 12 March 2020 survey. During WY 2021, mean snow depths showed a more varied trend. From 10 to 24 February, the mean snow depth and *twt* exhibited negligible change (−0.06 m, +0.08 ns), but derived density increased by +89 kg m^{-3}. During this interval, snow pit depth declined by −0.14 m and bulk snow density increased by +40 kg m^{-3} and, on 24 February, snow pit observations noted a surface wind crust (∼1 cm in height). These observations indicate that wind was a driving factor in the observed densification. Mean snow depths and *twt* increased between 24 February and 22 March (+0.34 m, +2.67 ns), but snow density decreased (−40 kg m^{-3}). This study year included a wet snow survey (27 May), where the mean snow depth declined by 53% relative to the 22 March survey. The mean and standard deviation of the 27 May relative permittivity (mean = 2.163, standard deviation = 0.444) were 1.3 and 2.5 times higher than the highest relative permittivity mean and standard deviation of the dry snow surveys (24 February 2021 mean = 1.695; 10 February 2021, standard deviation = 0.180).

The Ranch Creek survey explored the viability of UAV-borne lidar for snow depth retrieval in a shallower snowpack with both open and mixed conifer/deciduous forest cover. Derived relative permittivity uncertainty (0.418; Table S1) was within the range of relative permittivity uncertainties estimated for Cameron Pass surveys, despite having the lowest mean snow depth (0.62 m; Table S4). The mean relative permittivity value is only 0.043 less than the mean for the 27 May 2021 Cameron Pass survey, indicating similar mean LWC values for the two surveys, however, the standard deviation is much lower, indicating that LWC was more uniform in its distribution for the 7 April survey.

4.2 | Spatial variability of derived snow density and relative permittivity

Exponential variogram models (Figure 4) and corresponding experimental variograms (Figures S7–S10), indicate that nugget effects, or variability at scales smaller than the first lag distance, are absent from the snow depth, *twt*, and relative permittivity variogram models. A minor nugget effect (<1% of the overall variability) was estimated for the density variogram models, and a larger nugget effect (ranging from 2 to 7% of the total variability) was estimated for the SWE variogram models. Absent or very low nuggets indicate relatively low spatial variability (<10%) at the <10 m scale for these variables. Sills and correlation lengths are given for each of the variogram models in Table S5.

Variogram analysis reveals longer correlation lengths for snow depth and *twt* at Grand Mesa in the forests than in the open, with forests having a median difference of +6 m for snow depth and +11 m for *twt* (Figure 4a–e; Table S5). However, relative permittivity, snow density, and SWE have longer correlation lengths in the open than in the forests, with open environments having a median difference of +7 m for relative permittivity and snow density and +3 m for SWE. At Cameron Pass, no parameters revealed an obvious relation with time for WY 2020, but relative permittivity and snow density correlation lengths for WY 2021 decreased from 24 m on 10 February to 10 m on 22 March. Subsequently, the correlation length for relative permittivity increased substantially to 55 m during the wet snow survey on 27 May. A longer correlation length was also observed for relative permittivity on 7 April at Ranch Creek (34 m). These are two of the longest relative permittivity correlation lengths found in the study, indicating that wet snow may have longer correlation lengths for relative permittivity than dry snow.

4.3 | Evaluation of density models

Spatially distributed snow densities at Grand Mesa and Cameron Pass enable an evaluation of snow density models across a range of dates and snow conditions (Figure 5a–c). Here, we use the derived densities as a benchmark for comparison with modelled densities. A comparison between modelled densities and in-situ densities is available in Section A.4. Of the empirical models, J$_{09}$ yielded the lowest RMSE at both Grand Mesa (RMSE = 16 kg m^{-3}) and Cameron Pass (RMSE = 43 kg m^{-3}), whereas M&P$_{08}$ yielded large RMSEs at Cameron Pass (RMSE = 87 kg m^{-3}) and Grand Mesa (RMSE = 71 kg m^{-3}), and systematically underestimated snow density (mean difference = −75 kg m^{-3}). St$_{10}$ consistently overestimated snow density (mean difference = +37 kg m^{-3}). S&F$_{14}$ performed comparably to J$_{09}$ at Cameron Pass. We found that the variability from empirically estimated snow densities was more limited compared to derived (Figure 5a), and that empirical model accuracy decreased in lower snow depth conditions. SNODAS densities
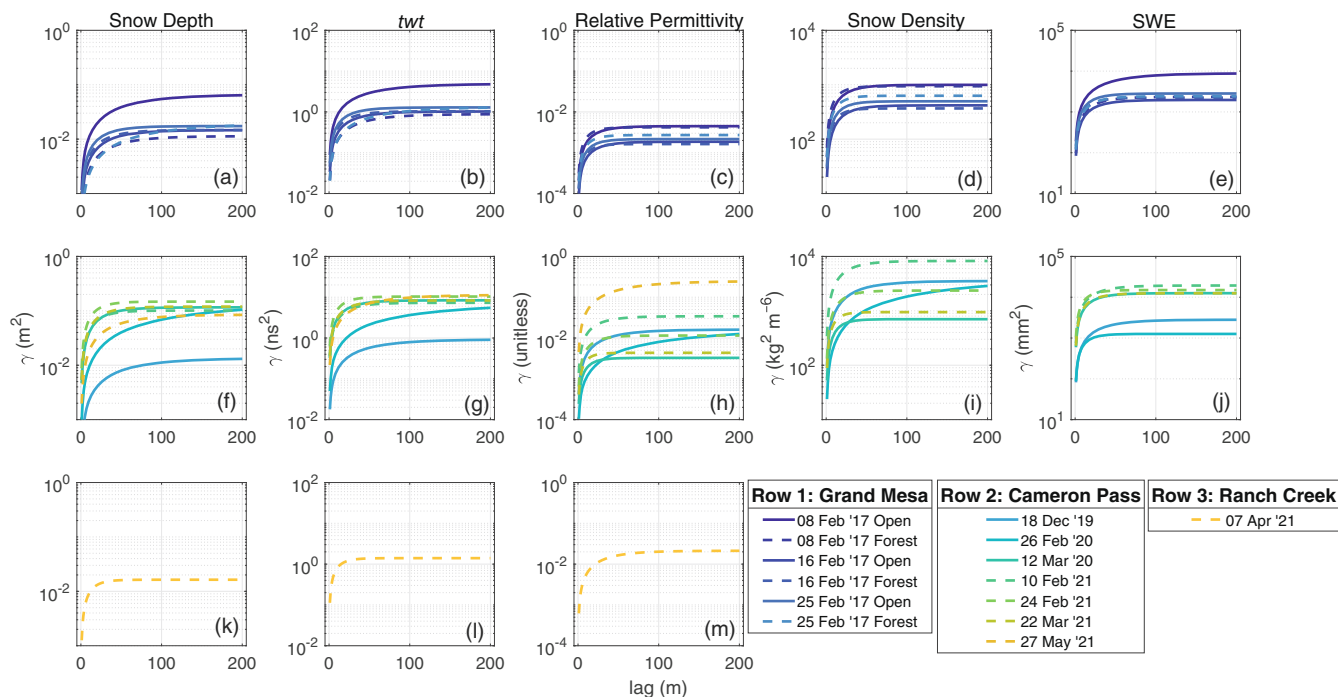
FIGURE 4 Exponential variogram models calculated from the best fit of the experimental variograms. Rows represent different field sites and are organized from top to bottom as (a–e) Grand Mesa, (f–j) Cameron Pass, and (k–m) Ranch Creek. Columns represent different variables and are organized from left to right as snow depth, *twt*, relative permittivity, snow density, and SWE.
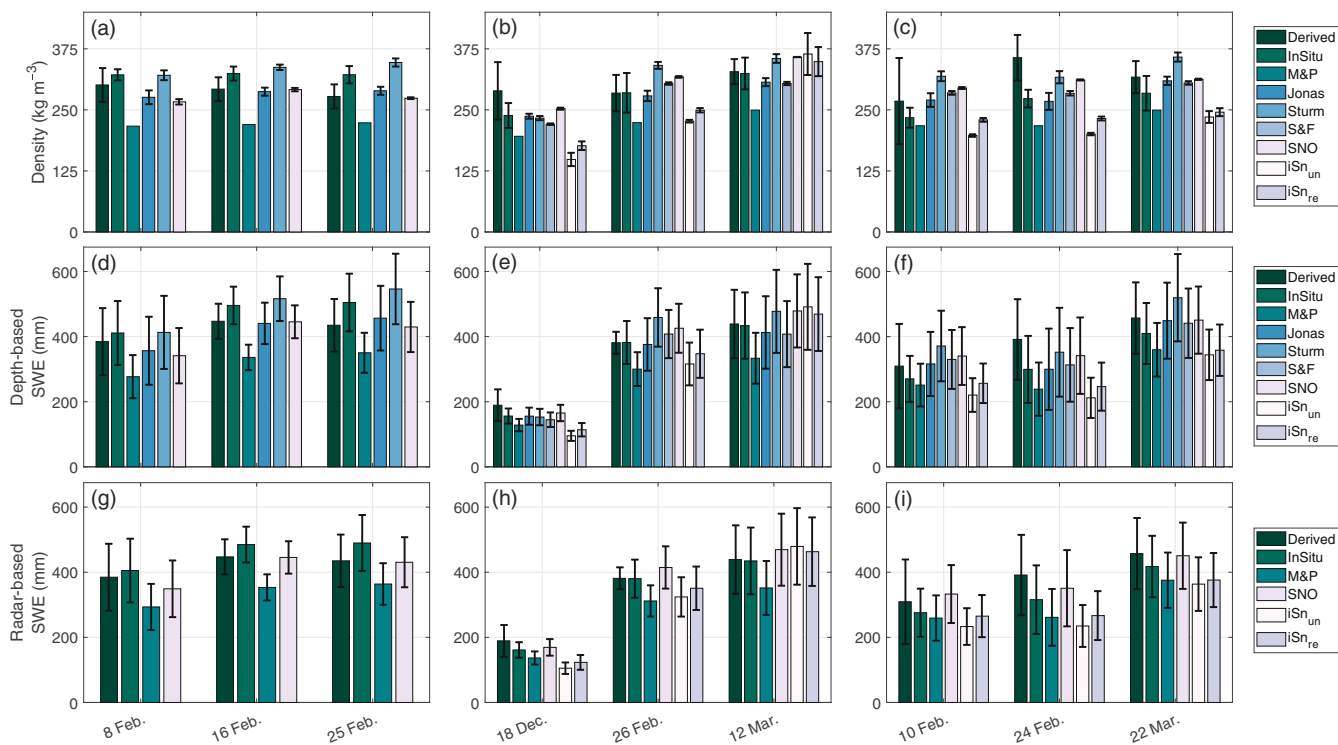
FIGURE 5 (a–c) Comparison between mean snow densities, (d–f) mean depth-based SWE, and (g–i) mean radar-based SWE estimated from the derived, in-situ, and modelled densities. Depth-based SWE was calculated using lidar snow depths, whereas radar-based SWE was calculated using *twt*. Columns are organized by field site, from left to right: Grand Mesa surveys from WY 2017, Cameron Pass surveys from WY 2020, and Cameron Pass surveys from WY 2021. Error bars show ±1 standard deviation. Depth-based empirical density models cannot be incorporated into radar-based SWE calculations and are thus absent in (g–i).

at Grand Mesa yielded an RMSE (20 kg m^{-3}) that was comparable to J$_{09}$, whereas SNODAS densities yielded the lowest RMSE (32 kg m^{-3}) at Cameron Pass. Unscaled iSnobal densities for Cameron Pass in WY 2020 yielded the highest RMSE (119 kg m^{-3}), whereas rescaled iSnobal densities improved the RMSE by 20 kg m^{-3}. iSnobal density accuracy improved for the March surveys, where RMSEs were 20%–60% lower than the overall RMSE. For both unscaled and rescaled iSnobal densities, estimates exhibited a substantial negative bias (mean residuals: iSn$_{un}$ = −85 kg m^{-3}, iSn$_{re}$ = −67 kg m^{-3}).

We then used the derived, modelled, and the mean of in-situ densities to calculate depth-based SWE from the lidar-measured snow depths (Figure 5d–f) and radar-based SWE from the GPR-measured *twt* (Figure 5g–i). We considered the SWE calculated from derived densities as the benchmark for this analysis. J$_{09}$ yielded the best performance for depth-based SWE estimates, estimating SWE within 10% for seven of nine surveys, whereas unscaled iSnobal yielded the largest errors, estimating depth-based and radar-based SWE within 20% for only two surveys. M&P$_{08}$ and rescaled iSnobal performed comparably: M&P$_{08}$ yielded two depth-based SWE surveys within 20% and five radar-based surveys within 20%, whereas rescaled iSnobal estimated depth-based and radar-based SWE within 20% for four surveys. M&P$_{08}$ did not produce SWE estimates within 10% for any survey, but rescaled iSnobal improved density estimates by an average of 7% and estimated depth-based and radar-based SWE within 10% for two surveys. St$_{10}$ estimated depth-based SWE within 10% for three of nine surveys, but yielded estimates within 20% for an additional five surveys. S&F$_{14}$ performed comparably to J$_{09}$ at Cameron Pass and estimated depth-based SWE within 10% for four surveys. SNODAS yielded the best overall performance for radar-based SWE, estimating SWE within 10% for eight of nine surveys, although its performance for depth-based SWE was reduced to four surveys within 10%. We found that the average in-situ density measurement yielded SWE within 10% for four of nine depth-based surveys and five of nine radar-based surveys.

5 | DISCUSSION

5.1 | Considerations for lidar-GPR surveys deriving relative permittivity and snow density

The combination of GPR and lidar for the derivation of snow densities or LWC is a promising method that could be employed to supplement in-situ methods for both operational surveys and large-scale snow campaigns (e.g., NASA SnowEx). From our study, we can compare the combination of different lidar platforms with different GPR survey designs (e.g., TLS with a transect GPR survey) to suggest 'best practices' for future studies. Combined lidar-GPR surveys for deriving relative permittivity need to consider the large uncertainty ranges that result from low snow depths (<1 m) and high snow depth uncertainty (>0.10 m; McGrath et al., 2022). We found that a spatial filter reduced the uncertainty range and yielded physically realistic densities, particularly when surveys were performed as grids or spirals. Spiral and grid

surveys have the added potential of spatial modeling to estimate relatively complete maps of relative permittivity and snow density in the surveyed region (e.g., Meehan, 2022). Airborne lidar platforms yielded lower snow depth uncertainties (±0.05 to ±0.08 m; Table S1) than the TLS (±0.07 to ±0.22 m), but the TLS snow depth uncertainty could be reduced substantially by surveying from a stable surface, rather than from a potentially shifting platform on the snow surface. Regardless of platform, we recommend that surveyors take careful notes regarding the GPR sled compression and the timing of the lidar collection relative to GPR surveys.

5.2 | Comparison with previous studies

The local-scale spatial variability of snow density is time consuming to measure using traditional in-situ sampling methods (López-Moreno et al., 2020). Therefore, snow density measurements tend to be sparser than other snow metrics, such as depth (Sturm et al., 2010), and thus density's spatial variability has seen few in-situ studies. We found that the average range in derived densities at Grand Mesa (135 kg m^{-3}) and Cameron Pass (179 kg m^{-3}; Figure 3, Figures S3–S5) compare favourably to the ranges in snow densities measured by in-situ studies conducted in the Spanish Pyrenees, where snow depths had a similar range to those measured in our study, but warmer temperatures led to rainfall during the winter of one study year (Fassnacht et al., 2010; López-Moreno et al., 2013). Density ranges up to 300 kg m^{-3} were observed from four snow density measurement campaigns conducted during accumulation (February 2010 and 2011) and around peak SWE (April 2010 and 2011) across three different locations ranging in elevation from 1517 to 3015 m (López-Moreno et al., 2013). Along a 5.4 km section of the Rio Esera in the Spanish Pyrenees, densities ranged from 350 to 450 kg m^{-3} in January 2009 (Fassnacht et al., 2010). The ranges reported by López-Moreno et al. (2013) fully encompass the maximum range observed in our derived density datasets, whereas Fassnacht et al. (2010) observed ranges more comparable to those we derived at Grand Mesa. It can be noted that, depending on the dominant processes, snowpack density can vary spatially at the 0.10 m scale (Fassnacht, 2021).

Several GPR-based methodologies have been developed to better understand the spatial distribution of snow densities and have increased the number of density estimates by two to three orders of magnitude compared to in-situ studies. However, GPR-based methodologies have generated snow density ranges that are physically unrealistic, especially when compared to in-situ measurements. Velocity migration analysis has derived densities with a large range (100–500 kg m^{-3}) along relatively short (∼100 m) transects in Wyoming's Medicine Bow Mountains (St. Clair & Holbrook, 2017), whereas multi-antenna pair GPR systems have derived densities as low as 150 kg m^{-3} during the melt season near Davos, Switzerland (Griessinger et al., 2018). Still, the multi-antenna pair methodology is promising; densities tended to range <80 kg m^{-3} for single ∼100 m transects for Griessinger et al. (2018), whereas another multi-antenna pair GPR system was used to derive a narrow range (370–420 kg m^{-3})

along a 78 km transect across the Greenland Ice Sheet (Meehan et al., 2021). Our approach differs in that it integrates independently measured snow depths with *twt* to derive permittivity and density, similar to Yildiz et al. (2021), who derived densities by combining UAV SfM snow depths with GPR in the Ilgaz Mountains, Turkey, and McGrath et al. (2022), who conducted a time series of UAV SfM snow depth/GPR surveys along a 150 m transect at a field site adjacent to Cameron Pass during the 2021 study year. However, our use of a spatial filter reduced the derived snow density standard deviation (21–88 kg m^{-3}; Table S4) by a factor of two, relative to Yildiz et al. (2021) and McGrath et al. (2022). Although the overall RMSE for our study is still high, the RMSE at Grand Mesa (45 kg m^{-3}) is lower than either of the UAV SfM/GPR studies (68–74 kg m^{-3}) and derived density ranges are physically realistic. Thus, as this method is further developed and tested, it may be used to provide unprecedented detail on the spatio-temporal distribution of snow densities.

5.3 | Spatial variability of snowpack parameters

Previous studies have shown that increases in average LWC are associated with larger LWC spatial variability and that radar-based methods for measuring SWE will have increased uncertainty when LWC is present in the snowpack (Bonnell et al., 2021; Webb et al., 2022). Although we do not estimate LWC, we identify a large shift between dry and wet relative permittivity sills (Table S5), indicating that relative permittivity variance is higher for wet snow surveys. However, we found increased correlation lengths during wet snow surveys, which seems counterintuitive, given the complicated spatial and temporal variability of LWC. The increased correlation length indicates that modeling bulk volumetric LWC may be possible for field sites that have little topographic complexity, such as Cameron Pass, and could reduce the uncertainty of SWE retrievals from radar-based methods.

Median correlation lengths were nearly identical for *twt* (27 m) and snow depth (30 m) and were lower than probed snow depth correlation lengths measured by Anderson et al. (2014) in southwest Idaho (median correlation length = 46 m). At Grand Mesa, median correlation lengths for snow depth and *twt* were longer in the forests than in the open, corroborating the findings of McGrath et al. (2019), who also found longer correlation lengths for probed depths and GPR-derived snow depths in the forest, but our mean correlation lengths in the open were nearly four times longer. Snow density and relative permittivity variograms yielded a median correlation length of 19 m, which is about twice that observed by Yildiz et al. (2021) but is much smaller than what López-Moreno et al. (2013) observed (<150 m). Experimental variograms of derived densities in Grand Mesa forests exhibited cyclicity at the sill level (Figure S7), possibly due to the snow accumulation dynamics in the forest islands of Grand Mesa (Webb, Raleigh, et al., 2020). Sills for derived relative permittivity and density at Cameron Pass (Figure 4, Figures S8 and S9) tended to be high in December and February and decrease with accumulation, where higher sills may result from snowpack variability induced by

topography and vegetation before the features are blanketed by snow.

5.4 | Model performance and selection

Of the empirical models, J$_{09}$ estimated densities and depth-based SWE with the lowest overall RMSE. St$_{10}$ showed a consistent, positive bias (Figure 5), which was also noted by McCreight and Small (2014), largely due to the DOY parameter, which is less sensitive to short-term fluctuations in snow density than the month parameter used by J$_{09}$. We found that the DOY-based M&P$_{08}$ systematically underestimated snow density and SWE at our sites, which could be improved for sites where calibration is an option (Pistocchi, 2016). J$_{09}$ estimated depth-based SWE within 10% for seven of the nine surveys and may represent a viable option for depth-based SWE remote sensing methods. Of the more complex models, SNODAS had a small negative bias across all surveys at Grand Mesa (overall mean residual = −14 kg m^{-3}) but exhibited no consistent bias for the Cameron Pass surveys, whereas unscaled and rescaled iSnobal densities were negatively biased for all Cameron Pass surveys (Figure 5). However, rescaling precipitation yielded improved iSnobal density estimates that exhibited lower RMSE (<50 kg m^{-3}) for WY 2020 surveys with deeper snowpacks (>1.30 m). Of all models, SNODAS yielded the most consistently accurate radar-based SWE (eight of nine surveys within 10%) and the second most consistently accurate depth-based SWE (nine of nine surveys within 15%), thus SNODAS may offer a suitable solution for snow density estimates in North America for both depth-based and radar-based methods.

Each evaluated model has known limitations. Empirical models are limited to a narrow, unrealistic range of density estimates (Raleigh & Small, 2017) and have been shown to decrease in accuracy with increased elevation (Avanzi & De Michele, 2015). Evaluations of SNODAS indicate that modelled SWE and snow depth have lower errors in subalpine regions (Clow et al., 2012; Dozier et al., 2016), but SNODAS tends to underestimate accumulation in deeper snowpacks (Hedrick et al., 2015) and may be unsuitable in alpine regions, where snow deposition and redistribution processes are more complex (Dozier et al., 2016). Accurate forcing data are necessary for robust iSnobal model output, but the HRRR precipitation forcing data used in our study was consistently lower than Joe Wright SNOTEL SWE for WY 2020 and 2021 (Figure S11). For WY 2021, HRRR precipitation underestimated SWE by >50%, which is a larger error than what Meyer et al. (2023) reported, and caused the substantially negative bias observed for estimated densities. Rescaling HRRR precipitation based on the 19 March 2021 Cameron Pass airborne lidar survey yielded more realistic spatial patterns for snow deposition but failed to generate accurate precipitation values at our field site, hence our introduced rescaling factor. Despite the higher RMSE values and biases, iSnobal remains a promising model for estimating snow densities, particularly where weather station coverage is sufficient or where HRRR precipitation is either accurate or can be corrected. As a final note, we found that lower SWE conditions (<300 mm) resulted in

larger percent errors from models, increasing the J_{09} and SNODAS SWE errors to 18% and 13%, respectively. St_{10} and $S\&F_{14}$ yielded SWE errors as high as 23%, whereas rescaled iSnobal SWE errors exceeded 30%. Thus, further evaluation of modelled densities in lower snow conditions is warranted.

6 | CONCLUSION

By combining GPR-measured *twt* with lidar-measured snow depths, we derived relative permittivity and snow density estimates along GPR transects at three sites during 11 surveys. For dry-snow surveys, this method yielded a mean RMSE of 54 kg m^{-3} (RMSE minimum = 45 kg m^{-3}, maximum = 92 kg m^{-3}) compared with nearby in-situ density measurements. At Grand Mesa, we observed that median correlation lengths for relative permittivity and density were 6 m longer in the open than in the forests, whereas at Cameron Pass, correlation lengths decreased by 10 m over the span of 1.5 months. We observed that relative permittivity has a higher variance in wet snow than in dry snow, but correlation lengths were longer for the wet snow surveys. We compared derived densities with densities estimated from four empirical models, SNODAS, and iSnobal and found that J_{09} was the most accurate density model for depth-based SWE retrievals (±10% for seven of nine surveys), whereas SNODAS densities yielded the most accurate SWE retrievals for radar-based methods (±10% for eight of nine surveys). However, for lower SWE environments (<300 mm) uncertainty increased to >20% for all models, which points to a potential issue in density modeling. Regardless, selecting an appropriate density model is difficult, and new models continue to be developed (e.g., Bisset et al., 2022; Meehan, 2022; Winkler et al., 2021). Empirical models evaluated in this study are directly applicable for depth-based SWE remote sensing methods and the Sentinel-1 co/cross-polarization backscatter method (Lievens et al., 2019, 2022), but site-specific calibration in both open and forested environments may improve results. Physically based models may be particularly powerful for InSAR methods of SWE retrieval, which can be applied over expansive regions (e.g., Oveisgharan et al., 2023) and require a surface density estimate to derive a change in SWE (Marshall et al., 2021), but these models are inherently limited by the chosen forcing data. With the increased availability of depth-based and radar-based remote sensing datasets, accurate density estimates are required to advance SWE remote sensing techniques. The accuracy and spatial coverage capabilities of the lidar-GPR snow density method makes it a promising avenue for model evaluation, training, and development.

CONFLICT OF INTEREST STATEMENT
The authors declare that they have no conflicts of interest.

DATA AVAILABILITY STATEMENT
Ground-penetrating radar (GPR) datasets for Grand Mesa (Webb et al., 2019; https://doi.org/10.5067/G21LGCNLFSC5) and Cameron Pass (McGrath et al., 2021; https://doi.org/10.5067/U4Q3X27BMRR4; Bonnell et al., 2022; https://doi.org/10.5067/SRWGLYCB6ZC4), Airborne Snow Observatory lidar datasets (Painter, 2018; https://doi.org/10.5067/KIE9QNVG7HP0), and snow pit measurements for Grand Mesa (Elder et al., 2018; https://doi.org/10.5067/Q0310G1XULZS) are archived at the NSIDC. The NSIDC has archived Cameron Pass 2020 snow pit measurements (Mason et al., 2023) and 2021 snow pit measurements are under review. Terrestrial lidar scan point clouds are archived with UNAVCO, Inc. (Williams, 2021; https://tls.unavco.org/projects/U-077/PS01/). Cameron Pass uncrewed aerial vehicle (UAV) lidar point cloud and bare earth digital elevation model and Ranch Creek UAV lidar point clouds and snow depth raster are archived with the U.S. Geological Survey (Bauer et al., 2023). Ranch Creek GPR surveys are archived at HydroShare (Bonnell & McGrath, 2023; https://doi.org/10.4211/hs.6f39721f1643428f84997f09ef75e2f8). SNOTEL station data (USDA Natural Resources Conservation Service, 2023) and Ranch Creek weather station data (U.S. Geological Survey, 2023) are available online. iSnobal/AWSM model code can be downloaded from https://github.com/USDA-ARS-NWRC/awsm/tree/master.

ORCID
Randall Bonnell https://orcid.org/0000-0002-8812-351X
Daniel McGrath https://orcid.org/0000-0002-9462-6842
Andrew R. Hedrick https://orcid.org/0000-0001-9511-1341
Graham Sexstone https://orcid.org/0000-0001-8913-0546
Ryan W. Webb https://orcid.org/0000-0002-1565-909X

REFERENCES

Adebisi, N., Marshall, H., Vuyovich, C. M., Elder, K., Hiemstra, C., & Durand, M. (2022). *SnowEx20-21 QSI lidar snow depth 0.5m UTM grid, version 1 [data set]*. NASA National Snow and Ice Data Center Distributed Active Archive Center. https://doi.org/10.5067/VBUN16K365DG

Alford, D. (1967). Density variations in alpine snow. *Journal of Glaciology*, 6(46), 495–503. https://doi.org/10.3189/S0022143000019717

Anderson, B. T., McNamara, J. P., Marshall, H.-P., & Flores, A. N. (2014). Insights into the physical processes controlling correlations between snow distribution and terrain properties. *Water Resources Research*, 50(6), 4545–4563. https://doi.org/10.1002/2013WR013714

Avanzi, F., & De Michele, C. (2015). On the performances of empirical regressions for the estimation of bulk snow density. *Geografia Fisica e Dinamica Quaternaria*, 38(2), 105–112. https://doi.org/10.4461/GFDQ.2015.38.10

Barnett, T. P., Adam, J. C., & Lettenmaier, D. P. (2005). Potential impacts of a warming climate on water availability in snow-dominated regions. *Nature*, 438(7066), 303–309. https://doi.org/10.1038/nature04141

Barrett, A. P. (2003). *National Operational Hydrologic Remote Sensing Center SNOw Data Assimilation System (SNODAS) products at NSIDC*. NSIDC Special Report 11. National Snow and Ice Data Center.

Bauer, M. A., Burgess, M. A., Adams, J. D., Sexstone, G. A., Fulton, J. W., McDermott, W. R., & Brady, L. R. (2023). *Lidar point clouds (LPCs), digital elevation models (DEMs), and snow depth raster maps derived from lidar data collected on small, uncrewed aircraft systems in the Upper Colorado River Basin, Colorado, 2020-22*. U.S. Geological Survey Data Release. https://doi.org/10.5066/P9LF15AE

Bisset, R., Floyd, B. C., Menounos, B., Bishop, A., Cebulski, A., Fisk, G., Marchenko, S., & Marshall, P. (2022). Quantifying spatio-temporally distributed snow density across four forested mountain watersheds in South-Western British Columbia. In *American Geophysical Union fall meeting 2022, Chicago, IL*. Poster.

Bonnell, R., & McGrath, D. (2023). *Ranch creek ground-penetrating radar snow survey April 07, 2021 [data set]*. HydroShare. https://doi.org/10.4211/hs.6f39721f1643428f84997f09ef75e2f8

Bonnell, R., McGrath, D., Williams, K., Webb, R., Fassnacht, S. R., & Marshall, H.-P. (2021). Spatiotemporal variations in liquid water content in a seasonal snowpack: Implications for radar remote sensing. *Remote Sensing*, 13(21), Article 21. https://doi.org/10.3390/rs13214223

Bonnell, R., McGrath, D., Zeller, L., Bump, E., & Olsen-Mikitowicz, A. (2022). *SnowEx21 Cameron pass ground penetrating radar, version 1 [data set]*. NASA National Snow and Ice Data Center Distributed Active Archive Center. https://doi.org/10.5067/SRWGLYCB6ZC4

Bonner, H. M., Raleigh, M. S., & Small, E. E. (2022). Isolating forest process effects on modelled snowpack density and snow water equivalent. *Hydrological Processes*, 36(1), e14475. https://doi.org/10.1002/hyp.14475

Bradford, J. H., Harper, J. T., & Brown, J. (2009). Complex dielectric permittivity measurements from ground-penetrating radar data to estimate snow liquid water content in the pendular regime. *Water Resources Research*, 45(8), W08403. https://doi.org/10.1029/2008WR007341

Broxton, P. D., Zeng, X., & Dawson, N. (2016). Why do global Reanalyses and land data assimilation products underestimate snow water equivalent? *Journal of Hydrometeorology*, 17(11), 2743–2761. https://doi.org/10.1175/JHM-D-16-0056.1

Clow, D. W., Nanus, L., Verdin, K. L., & Schmidt, J. (2012). Evaluation of SNODAS snow depth and snow water equivalent estimates for the Colorado Rocky Mountains, USA. *Hydrological Processes*, 26(17), 2583–2591. https://doi.org/10.1002/hyp.9385

Currier, W. R., Pflug, J., Mazzotti, G., Jonas, T., Deems, J. S., Bormann, K. J., Painter, T. H., Hiemstra, C. A., Gelvin, A., Uhlmann, Z., Spaete, L., Glenn, N. F., & Lundquist, J. D. (2019). Comparing aerial lidar observations with terrestrial lidar and snow-probe transects from NASA's 2017 SnowEx campaign. *Water Resources Research*, 55(7), 6285–6294. https://doi.org/10.1029/2018WR024533

Daniels, D. J. (Ed.). (2004). *Ground penetrating radar* (Vol. 1). The Institution of Electrical Engineers.

Deeb, E. J., Forster, R. R., & Kane, D. L. (2011). Monitoring snowpack evolution using interferometric synthetic aperture radar on the north slope of Alaska, USA. *International Journal of Remote Sensing*, 32(14), 3985–4003. https://doi.org/10.1080/01431161003801351

Deems, J. S., Painter, T. H., & Finnegan, D. C. (2013). Lidar measurement of snow depth: A review. *Journal of Glaciology*, 59(215), 467–479. https://doi.org/10.3189/2013JoG12J154

Di Paolo, F., Cosciotti, B., Lauro, S. E., Mattei, E., & Pettinelli, E. (2020). A critical analysis on the uncertainty computation in ground-penetrating radar-retrieved dry snow parameters. *Geophysics*, 85(4), H39–H49. https://doi.org/10.1190/geo2019-0683.1

Dietz, A. J., Kuenzer, C., Gessner, U., & Dech, S. (2012). Remote sensing of snow – A review of available methods. *International Journal of Remote Sensing*, 33(13), 4094–4134. https://doi.org/10.1080/01431161.2011.640964

Dozier, J., Bair, E. H., & Davis, R. E. (2016). Estimating the spatial distribution of snow water equivalent in the world's mountains. *WIREs Water*, 3(3), 461–474. https://doi.org/10.1002/wat2.1140

Durand, M., Gatebe, C., Kim, E., Molotch, N., Painter, T. H., Raleigh, M., Sandells, M., & Vuyovich, C. (2018). *NASA SnowEx Science Plan: Assessing approaches for measuring water in Earth's Seasonal Snow, version 1.6*.

Elder, K., Brucker, L., Hiemstra, C., & Marshall, H. (2018). *SnowEx17 community snow pit measurements, version 1 [data set]*. NASA National Snow and Ice Data Center Distributed Active Archive Center. https://doi.org/10.5067/Q0310G1XULZS

Enderlin, E. M., Elkin, C. M., Gendreau, M., Marshall, H. P., O'Neel, S., McNeil, C., Florentine, C., & Sass, L. (2022). Uncertainty of ICESat-2 ATL06- and ATL08-derived snow depths for glacierized and vegetated mountain regions. *Remote Sensing of Environment*, 283, 113307. https://doi.org/10.1016/j.rse.2022.113307

ESRI. (2023). *ArcGIS Pro v3.1.2* [Software]. https://www.esri.com/en-us/arcgis/products/arcgis-pro/overview

Fassnacht, S. R. (2021). A call for more snow sampling. *Geosciences*, 11, 435. https://doi.org/10.3390/geosciences11110435

Fassnacht, S. R., Brown, K. S. J., Blumberg, E. J., López-Moreno, J. I., Covino, T. P., Kappas, M., Huang, Y., Leone, V., & Kashipazha, A. H. (2018). Distribution of snow depth variability. *Frontiers of Earth Science*, 12, 683–692. https://doi.org/10.1007/s11707-018-0714-z

Fassnacht, S. R., Heun, C. M., López-Moreno, J. I., & Latron, J. (2010). Snow density variability in the Rio Esera Valley, Pyrenees Mountains, Spain. In *Hydrology days 2010*. Paper.

Griessinger, N., Mohr, F., & Jonas, T. (2018). Measuring snow ablation rates in alpine terrain with a mobile multioffset ground-penetrating radar system. *Hydrological Processes*, 32(21), 3272–3282. https://doi.org/10.1002/hyp.13259

Guneriussen, T., Hogda, K. A., Johnsen, H., & Lauknes, I. (2001). InSAR for estimation of changes in snow water equivalent of dry snow. *IEEE Transactions on Geoscience and Remote Sensing*, 39(10), 2101–2108. https://doi.org/10.1109/36.957273

Hale, K., Kiewiet, L., Trujillow, E., Krohe, C., Hedrick, A., Marks, D., Kormos, P., Havens, S., McNamara, J., Link, T., & Godsey, S. E. (2023). Drivers of spatiotemporal patterns of surface water inputs in a catchment at the rain-snow transition zone of the water-limited western United States. *Journal of Hydrology*, 616, 128699. https://doi.org/10.1016/j.jhydrol.2022.128699

Hammond, J. C., Saavedra, F. A., & Kampf, S. K. (2018). Global snow zone maps and trends in snow persistence 2001–2016. *International Journal of Climatology*, 38(12), 4369–4383. https://doi.org/10.1002/joc.5674

Havens, S., Marks, D., Sandusky, M., Hedrick, A., Johnson, M., Robertson, M., & Trujillo, E. (2020). Automated water supply model

(AWSM): Streamlining and standardizing application of a physically based snow model for water resources and reproducible science. *Computers & Geosciences*, *144*, 104571. https://doi.org/10.1016/j.cageo.2020.104571

Hedrick, A., Marshall, H.-P., Winstral, A., Elder, K., Yueh, S., & Cline, D. (2015). Independent evaluation of the SNODAS snow depth product using regional-scale lidar-derived measurements. *The Cryosphere*, *9*(1), 13–23. https://doi.org/10.5194/tc-9-13-2015

Hedrick, A. R., Marks, D., Havens, S., Robertson, M., Johnson, M., Sandusky, M., Marshall, H.-P., Kormos, P. R., Bormann, K. J., & Painter, T. H. (2018). Direct insertion of NASA airborne snow observatory-derived snow depth time series into the iSnobal energy balance snow model. *Water Resources Research*, *54*(10), 8045–8063. https://doi.org/10.1029/2018WR023190

Heilig, A., Mitterer, C., Schmid, L., Wever, N., Schweizer, J., Marshall, H.-P., & Eisen, O. (2015). Seasonal and diurnal cycles of liquid water in snow—Measurements and modeling. *Journal of Geophysical Research: Earth Surface*, *120*(10), 2139–2154. https://doi.org/10.1002/2015JF003593

Huckaby, L. S., & Moir, W. H. (1998). *Forest communities at Fraser experimental forest, Colorado* (pp. 204–218). The Southwestern Naturalist.

Isaaks, E. H., & Srivastava, R. M. (1989). *Applied geostatistics* (Vol. 561). Oxford University Press.

Jonas, T., Marty, C., & Magnusson, J. (2009). Estimating the snow water equivalent from snow depth measurements in the Swiss Alps. *Journal of Hydrology*, *378*(1), 161–167. https://doi.org/10.1016/j.jhydrol.2009.09.021

Kiewiet, L., Trujillow, E., Hedrick, A., Havens, S., Hale, K., Seyfried, M., Kampf, S., & Godsey, S. (2022). Effects of spatial and temporal variability in surface water inputs on streamflow generation and cessation in the rain–snow transition zone. *Hydrology and Earth System Sciences*, *26*(10), 2779–2796. https://doi.org/10.5194/hess-26-2779-2022

Kim, E. (2018). How can we find out how much snow is in the world? *Eos*, *99*. http://eos.org/science-updates/how-can-we-find-out-how-much-snow-is-in-the-world

Koch, F., Prasch, M., Schmid, L., Schweizer, J., & Mauser, W. (2014). Measuring snow liquid water content with low-cost GPS receivers. *Sensors*, *14*(11), 20975–20999. https://doi.org/10.3390/s141120975

Kovacs, A., Gow, A. J., & Morey, R. M. (1995). The in-situ dielectric constant of polar firn revisited. *Cold Regions Science and Technology*, *23*(3), 245–256. https://doi.org/10.1016/0165-232X(94)00016-Q

Kuroiwa, D. (1954). *The dielectric property of snow*. International Association of Hydrological Sciences Publication.

Largeron, C., Dumont, M., Morin, S., Boone, A., Lafaysse, M., Metref, S., Cosme, E., Jonas, T., Winstral, A., & Margulis, S. A. (2020). Toward snow cover estimation in mountainous areas using modern data assimilation methods: A review. *Frontiers in Earth Science*, *8*, 325. https://doi.org/10.3389/feart.2020.00325

Lehning, M., Bartelt, P., Brown, B., & Fierz, C. (2002). A physical SNOWPACK model for the Swiss avalanche warning: Part III: Meteorological forcing, thin layer formation and evaluation. *Cold Regions Science and Technology*, *35*(3), 169–184. https://doi.org/10.1016/S0165-232X(02)00072-1

Lehning, M., Bartelt, P., Brown, B., Fierz, C., & Satyawali, P. (2002). A physical SNOWPACK model for the Swiss avalanche warning: Part II: Snow microstructure. *Cold Regions Science and Technology*, *35*(3), 147–167. https://doi.org/10.1016/S0165-232X(02)00073-3

Lievens, H., Brangers, I., Marshall, H.-P., Jonas, T., Olefs, M., & De Lannoy, G. (2022). Sentinel-1 snow depth retrieval at sub-kilometer resolution over the European Alps. *The Cryosphere*, *16*(1), 159–177. https://doi.org/10.5194/tc-16-159-2022

Lievens, H., Demuzere, M., Marshall, H.-P., Reichle, R. H., Brucker, L., Brangers, I., de Rosnay, P., Dumont, M., Girotto, M., Immerzeel, W. W., Jonas, T., Kim, E. J., Koch, I., Marty, C., Saloranta, T., Schöber, J., & De Lannoy, G. J. M. (2019). Snow depth variability in the northern hemisphere mountains observed from space. *Nature Communications*, *10*(1), Article 1. https://doi.org/10.1038/s41467-019-12566-y

López-Moreno, J. I., Fassnacht, S. R., Heath, J. T., Musselman, K. N., Revuelto, J., Latron, J., Morán-Tejeda, E., & Jonas, T. (2013). Small scale spatial variability of snow density and depth over complex alpine terrain: Implications for estimating snow water equivalent. *Advances in Water Resources*, *55*, 40–52. https://doi.org/10.1016/j.advwatres.2012.08.010

López-Moreno, J. I., Leppänen, L., Luks, B., Holko, L., Picard, G., Sanmiguel-Vallelado, A., Alons-González, E., Finger, D. C., Arslan, A. N., Gillemot, K., Sensory, A., Sorman, A., Ertas, M. C., Fassnacht, S. R., Fierz, C., & Marty, C. (2020). Intercomparison of measurements of bulk snow density and water equivalent of snow cover with snow core samplers: Instrumental bias and variability induced by observers. *Hydrological Processes*, *34*, 3120–3133. https://doi.org/10.1002/hyp.13785

Lundberg, A., Richardson-Näslund, C., & Andersson, C. (2006). Snow density variations: Consequences for ground-penetrating radar. *Hydrological Processes*, *20*(7), 1483–1495. https://doi.org/10.1002/hyp.5944

Lv, Z., Pomeroy, J., & Fang, X. (2019). Evaluation of SNODAS snow water equivalent in Western Canada and assimilation into a cold region hydrological model. *Water Resources Research*, *55*(12), 11166–11187. https://doi.org/10.1029/2019WR025333

Mankin, J. S., Viviroli, D., Singh, D., Hoekstra, A. Y., & Diffenbaugh, N. S. (2015). The potential for snow to supply human water demand in the present and future. *Environmental Research Letters*, *10*(11), 114016. https://doi.org/10.1088/1748-9326/10/11/114016

Marks, D., Domingo, J., Susong, D., Link, T., & Garen, D. (1999). A spatially distributed energy balance snowmelt model for application in mountain basins. *Hydrological Processes*, *13*(12–13), 1935–1959. https://doi.org/10.1002/(SICI)1099-1085(199909)13:12/13<1935::AID-HYP868>3.0.CO;2-C

Marshall, H. P., Deeb, E., Forster, R., Vuyovich, C., Elder, K., Hiemstra, C., & Lund, J. (2021). L-band InSAR depth retrieval during the NASA SnowEx 2020 campaign: Grand Mesa, Colorado. In *2021 IEEE international geoscience and remote sensing symposium, IGARSS* (pp. 625–627). https://doi.org/10.1109/IGARSS47720.2021.9553852

Marshall, H.-P., Koh, G., & Forster, R. R. (2005). Estimating alpine snowpack properties using FMCW radar. *Annals of Glaciology*, *40*, 157–162. https://doi.org/10.3189/172756405781813500

Marshall, H.-P., Vuyovich, C., Hiemstra, C., Brucker, L., Elder, K., Deems, J., & Newlin, J. (2019). *NASA SnowEx 2020 experiment plan*. Science Plan.

Mason, M., Marhsall, H., McCormick, M., Craaybeek, D., Elder, K., & Vuyovich, C. M. (2023). *SnowEx20 time series snow pit measurements, version 1 [data set]*. NASA National Snow and Ice Data Center Distributed Active Archive Center. https://doi.org/10.5067/POT9E0FFUUD1

McCreight, J. L., & Small, E. E. (2014). Modeling bulk density and snow water equivalent using daily snow depth observations. *The Cryosphere*, *8*(2), 521–536. https://doi.org/10.5194/tc-8-521-2014

McGrath, D., Bonnell, R., Olsen-Mikitowicz, A., Duncan, C., & Grabowski, J. (2021). *SnowEx20 Cameron pass ground penetrating radar, version 1 [data set]*. NASA National Snow and Ice Data Center Distributed Active Archive Center. https://doi.org/10.5067/U4Q3X27BMRR4

McGrath, D., Bonnell, R., Zeller, L., Olsen-Mikitowicz, A., Bump, E., Webb, R., & Marshall, H.-P. (2022). A time series of snow density and snow water equivalent observations derived from the integration of GPR and UAV SfM observations. *Frontiers in Remote Sensing*, *3*, 886747. https://doi.org/10.3389/frsen.2022.886747

McGrath, D., Webb, R., Shean, D., Bonnell, R., Marshall, H.-P., Painter, T. H., Molotch, N. P., Elder, K., Hiemstra, C., & Brucker, L. (2019). Spatially extensive ground-penetrating radar snow depth observations during NASA's 2017 SnowEx campaign: Comparison

with In situ, airborne, and satellite observations. *Water Resources Research*, *55*(11), 10026–10036. https://doi.org/10.1029/2019WR024907

Meehan, T. G. (2022). *Advancements in measuring and modeling the mechanical and hydrological properties of snow and firn: Multi-sensor analysis, integration, and algorithm development*. Boise State University Theses and Dissertations. https://doi.org/10.18122/td.1979.boisestate

Meehan, T. G., Marshall, H. P., Bradford, J. H., Hawley, R. L., Overly, T. B., Lewis, G., Graeter, K., Osterberg, E., & McCarthy, F. (2021). Reconstruction of historical surface mass balance, 1984–2017 from GreenTrACS multi-offset ground-penetrating radar. *Journal of Glaciology*, *67*(262), 219–228. https://doi.org/10.1017/jog.2020.91

Meyer, J., Hotel, J., Kormos, P., Hedrick, A., Trujillo, E., & Skiles, S. M. (2023). Operational water forecast ability of the HRRR-iSnobal combination: An evaluation to adapt into production environments. *Geoscientific Model Development*, *16*(1), 233–250. https://doi.org/10.5194/gmd-16-233-2023

Mizukami, N., & Perica, S. (2008). Spatiotemporal characteristics of snowpack density in the mountainous regions of the Western United States. *Journal of Hydrometeorology*, *9*(6), 1416–1426. https://doi.org/10.1175/2008JHM981.1

Moller, D., Andreadis, K. M., Bormann, K. J., Hensley, S., & Painter, T. H. (2017). Mapping snow depth from ka-band interferometry: Proof of concept and comparison with scanning lidar retrievals. *IEEE Geoscience and Remote Sensing Letters*, *14*(6), 886–890. https://doi.org/10.1109/LGRS.2017.2686398

Moore, C., Kampf, S., Stone, B., & Richer, E. (2015). A GIS-based method for defining snow zones: Applications to the western United States. *Geocarto International*, *30*(1), 62–82. https://doi.org/10.1080/10106049.2014.885089

Mote, P. W., Li, S., Lettenmaier, D. P., Xiao, M., & Engel, R. (2018). Dramatic declines in snowpack in the western US. *Npj Climate and Atmospheric Science*, *1*(1), Article 1. https://doi.org/10.1038/s41612-018-0012-1

National Academies of Sciences, Engineering, and Medicine. (2018). *Thriving on our changing planet: A decadal strategy for earth observation from space*. National Academies Press. https://doi.org/10.17226/24938

Nolin, A. W. (2010). Recent advances in remote sensing of seasonal snow. *Journal of Glaciology*, *56*(200), 1141–1150. https://doi.org/10.3189/002214311796406077

Oveisgharan, S., Zinke, R., Hoppinen, Z., & Marshall, H. P. (2023). Snow water equivalent retrieval over Idaho, part a: Using Sentinel-1 repeat-pass interferometry. *The Cryosphere Discussions*, *2023*, 1–19. https://doi.org/10.5194/tc-2023-95

Painter, T. (2018). *ASO L4 lidar snow depth 3m UTM grid, version 1 [data set]*. NASA National Snow and Ice Data Center Distributed Active Archive Center. https://doi.org/10.5067/KIE9QNVG7HP0

Painter, T. H., Berisford, D. F., Boardman, J. W., Bormann, K. J., Deems, J. S., Gehrke, F., Hedrick, A., Joyce, M., Laidlaw, R., Marks, D., Mattmann, C., McGurk, B., Ramirez, P., Richardson, M., Skiles, S. M., Seidel, F. C., & Winstral, A. (2016). The airborne snow observatory: Fusion of scanning lidar, imaging spectrometer, and physically-based modeling for mapping snow water equivalent and snow albedo. *Remote Sensing of Environment*, *184*, 139–152. https://doi.org/10.1016/j.rse.2016.06.018

Painter, T. H., & Bormann, K. J. (2020). *ASO L4 lidar point cloud digital terrain model 3m UTM grid, version 1 [data set]*. NASA National Snow and Ice Data Center Distributed Active Archive Center. https://doi.org/10.5067/2EHMWG4IT760

Pistocchi, A. (2016). Simple estimation of snow density in an alpine region. *Journal of Hydrology: Regional Studies*, *6*, 82–89. https://doi.org/10.1016/j.ejrh.2016.03.004

Raleigh, M. S., & Small, E. E. (2017). Snowpack density modeling is the primary source of uncertainty when mapping basin-wide SWE with lidar. *Geophysical Research Letters*, *44*(8), 3700–3709. https://doi.org/10.1002/2016GL071999

Schwanghart, W. (2022a). *Experimental (semi-) variogram (version 1.4.0.0)*. MATLAB Central File Exchange. https://www.mathworks.com/matlabcentral/fileexchange/20355-experimental-semi-variogram

Schwanghart, W. (2022b). *variogramfit (Version 1.5.0.0)*. MATLAB Central File Exchange. https://www.mathworks.com/matlabcentral/fileexchange/25948-variogramfit

Sexstone, G. A., & Fassnacht, S. R. (2014). What drives basin scale spatial variability of snowpack properties in northern Colorado? *The Cryosphere*, *8*(2), 329–344. https://doi.org/10.5194/tc-8-329-2014

Shean, D. E., Alexandrov, O., Moratto, Z. M., Smith, B. E., Joughin, I. R., Porter, C., & Morin, P. (2016). An automated, open-source pipeline for mass production of digital elevation models (DEMs) from very-high-resolution commercial stereo satellite imagery. *ISPRS Journal of Photogrammetry and Remote Sensing*, *116*, 101–117. https://doi.org/10.1016/j.isprsjprs.2016.03.012

Shi, J., Xiong, C., & Jiang, L. (2016). Review of snow water equivalent microwave remote sensing. *Science China Earth Sciences*, *59*(4), 731–745. https://doi.org/10.1007/s11430-015-5225-0

Shook, K., & Gray, D. M. (1996). Small-scale spatial structure of shallow Snowcovers. *Hydrological Processes*, *10*(10), 1283–1292. https://doi.org/10.1002/(SICI)1099-1085(199610)10:10<1283::AID-HYP460>3.0.CO;2-M

Siirila-Woodburn, E. R., Rhoades, A. M., Hatchett, B. J., Huning, L. S., Szinai, J., Tague, C., Nico, P. S., Feldman, D. R., Jones, A. D., Collins, W. D., & Kaatz, L. (2021). A low-to-no snow future and its impacts on water resources in the western United States. *Nature Reviews Earth & Environment*, *2*(11), Article 11. https://doi.org/10.1038/s43017-021-00219-y

St. Clair, J., & Holbrook, W. S. (2017). Measuring snow water equivalent from common-offset GPR records through migration velocity analysis. *The Cryosphere*, *11*(6), 2997–3009. https://doi.org/10.5194/tc-11-2997-2017

Sturm, M. (2015). White water: Fifty years of snow research in WRR and the outlook for the future. *Water Resources Research*, *51*(7), 4948–4965. https://doi.org/10.1002/2015WR017242

Sturm, M., Holmgren, J., & Liston, G. E. (1995). A seasonal snow cover classification system for local to global applications. *Journal of Climate*, *8*(5), 1261–1283. https://doi.org/10.1175/1520-0442(1995)008<1261:ASSCCS>2.0.CO;2

Sturm, M., Taras, B., Liston, G. E., Derksen, C., Jonas, T., & Lea, J. (2010). Estimating snow water equivalent using snow depth data and climate classes. *Journal of Hydrometeorology*, *11*(6), 1380–1394. https://doi.org/10.1175/2010JHM1202.1

Susong, D., Marks, D., & Garen, D. (1999). Methods for developing time-series climate surfaces to drive topographically distributed energy- and water-balance models. *Hydrological Processes*, *13*(12–13), 2003–2021.

Tarricone, J., Webb, R. W., Marshall, H. P., Nolin, A. W., & Meyer, F. J. (2023). Estimating snow accumulation and ablation with L-band interferometric synthetic aperture radar. *The Cryosphere*, *17*(5), 1997–2019. https://doi.org/10.5194/tc-1997-2023

Techel, F., & Pielmeier, C. (2011). Point observations of liquid water content in wet snow – Investigating methodical, spatial and temporal aspects. *The Cryosphere*, *5*(2), 405–418. https://doi.org/10.5194/tc-5-405-2011

Tsang, L., Durand, M., Derksen, C., Barros, A. P., Kang, D.-H., Lievens, H., Marshall, H.-P., Zhu, J., Johnson, J., King, J., Lemmetyinen, J., Sandells, M., Rutter, N., Siqueira, P., Nolin, A., Osmanoglu, B.,

Vuyovich, C., Kim, E., Taylor, D., … Xu, X. (2022). Review article: Global monitoring of snow water equivalent using high-frequency radar remote sensing. *The Cryosphere*, 16(9), 3531–3573. https://doi.org/10.5194/tc-16-3531-2022

U.S. Geological Survey. (2023). *USGS water data for the nation [data set]*. National Water Information System data available on the World Wide Web. https://doi.org/10.5066/F7P55KJN

USDA Natural Resources Conservation Service. (2023). *SNOwpack TELemetry network (SNOTEL) [data set]*. NRCS. https://data.nal.usda.gov/dataset/snowpack-telemetry-network-snotel

Voegeli, C., Lehning, M., Wever, N., & Bavay, M. (2016). Scaling precipitation input to spatially distributed hydrological models by measured snow distribution. *Frontiers in Earth Science*, 4, 108. https://doi.org/10.3389/feart.2016.00108

Webb, R., McGrath, D., Hale, K., & Molotch, N. P. (2019). *SnowEx17 ground penetrating radar, version 2 [data set]*. NASA National Snow and Ice Data Center Distributed Active Archive Center. https://doi.org/10.5067/G21LGCNLFSC5

Webb, R. W., Jennings, K. S., Fend, M., & Molotch, N. P. (2018). Combining ground-penetrating radar with terrestrial LiDAR scanning to estimate the spatial distribution of liquid water content in seasonal snowpacks. *Water Resources Research*, 54(12), 10339–10349. https://doi.org/10.1029/2018WR022680

Webb, R. W., Marziliano, A., McGrath, D., Bonnell, R., Meehan, T. G., Vuyovich, C., & Marshall, H. P. (2021). In situ determination of dry and wet snow permittivity: Improving equations for low frequency radar applications. *Remote Sensing*, 13(22), 4617. https://doi.org/10.3390/rs13224617

Webb, R. W., Musselman, K. N., Ciafone, S., Hale, K. E., & Molotch, N. P. (2022). Extending the vadose zone: Characterizing the role of snow for liquid water storage and transmission in streamflow generation. *Hydrological Processes*, 36(3), e14541. https://doi.org/10.1002/hyp.14541

Webb, R. W., Raleigh, M. S., McGrath, D., Molotch, N. P., Elder, K., Hiemstra, C., Brucker, L., & Marshall, H. P. (2020). Within-stand boundary effects on snow water equivalent distribution in forested areas. *Water Resources Research*, 56(10), e2019WR024905. https://doi.org/10.1029/2019WR024905

Webb, R. W., Wigmore, O., Jennings, K., Fend, M., & Molotch, N. P. (2020). Hydrologic connectivity at the hillslope scale through intra-snowpack flow paths during snowmelt. *Hydrological Processes*, 34(7), 1616–1629. https://doi.org/10.1002/hyp.13686

Webster, R., & Oliver, M. A. (2001). *Geostatistics for environmental scientists*. John Wiley.

Williams, K. (2021). *Cameron pass NASA SnowEx [data set]*. UNAVCO Inc. https://tls.unavco.org/projects/U-077/

Winkler, M., Schellander, H., & Gruber, S. (2021). Snow water equivalents exclusively from snow depths and their temporal changes: The ΔSNOW model. *Hydrology and Earth System Sciences*, 25(3), 1165–1187. https://doi.org/10.5194/hess-25-1165-2021

Wrzesien, M. L., Durand, M. T., Pavelsky, T. M., Kapnick, S. B., Zhang, Y., Guo, J., & Shum, C. K. (2018). A new estimate of north American Mountain snow accumulation from regional climate model simulations. *Geophysical Research Letters*, 45(3), 1423–1432. https://doi.org/10.1002/2017GL076664

Yildiz, S., Akyurek, Z., & Binley, A. (2021). Quantifying snow water equivalent using terrestrial ground penetrating radar and unmanned aerial vehicle photogrammetry. *Hydrological Processes*, 35(5), e14190. https://doi.org/10.1002/hyp.14190

SUPPORTING INFORMATION

Additional supporting information can be found online in the Supporting Information section at the end of this article.

APPENDIX A: Detailed Methods

A.1 | Lidar and Ground-Penetrating Radar Data Processing

During surveys, lidar-measured snow depths were collected from one of three platforms (airborne, terrestrial, and uncrewed aerial vehicle). The Airborne Snow Observatory (ASO) processed snow-free and snow-on lidar elevation point clouds, producing 3 m snow depth rasters (Painter et al., 2016). U.S. Geological Survey (USGS) processed snow-free and snow-on uncrewed aerial vehicle (UAV) lidar point clouds and produced bare earth and snow depth rasters at 0.10 m spatial resolution (Bauer et al., 2023). USGS rasters were subsequently rescaled to 3 m spatial resolution. Terrestrial lidar scan (TLS) point clouds were accessed from UNAVCO, Inc. (Williams, 2021), filtered, aligned, and projected (Table 1) to align with the snow-free digital terrain model (DTM) collected by the USGS. For each lidar dataset, the snow surface was identified and point returns from vegetation were removed in ArcGIS Pro v3.1.2 (ESRI, 2023). The lidar datasets were converted to raster format with 3 m resolution using the average point elevation per cell. The snow-on rasters were aligned with the snow-free raster using the mean elevation difference between the snow-on and snow-free rasters from a 0.7 km section of snow-free highway (CO-14) that parallels the study area. The snow-free raster was then differenced from the snow-on scans to produce snow depth rasters. We assumed the road that bounds the meadow (Highway CO-14) had the same elevation for all scans and we estimated snow depth uncertainty as the standard deviation of the differences in elevation between the snow-on and snow-free rasters along the road. Finally, because lidar scans were performed after ground-penetrating radar (GPR) surveys, each snow depth raster received a +0.02–0.05 m adjustment based on field notes of average snow surface compression from the GPR sled.

GPR radargrams were collected as common-offset surveys via a sled coupled to the snow surface. Grand Mesa GPR surveys used a 1.6 GHz center-frequency Mala ProEx GPR, whereas surveys at the other two sites used a 1.0 GHz center-frequency Sensors & Software PulseEkko GPR. Both GPR units operated in free run and collected traces at 5–10 Hz. Radargram processing followed a general workflow: (1) geolocate traces (spatial accuracy = ±0.25 m), (2) time-zero correction, (3) remove DC-shift (dewow), (4) equidistant trace interpolation to 0.10 m, (5) 2-dimensional filtering to remove instrument noise, and (6) picking the ground reflection two-way travel time.

Additional processing notes are provided in the User Documentation for each published GPR dataset (Webb et al., 2019; McGrath et al., 2021; Bonnell et al., 2022).

A.2 | Identifying Dry and Wet Snow Conditions

Surveys were identified as dry snow based on notes and temperatures taken in snow pits (Figure S2). A number of snow pit surveys at Grand Mesa (Elder et al., 2018) noted the presence of LWC using the hand squeeze test (Techel & Pielmeier, 2011), but the snow temperature measurements seemingly contradict these observations. Although near-surface (< 30 cm depth) snow layers had a median temperature of − 1°C on 10 February, the deeper layers had a median temperature of − 2°C and, given the accuracy of the thermometers (± 0.5°C), indicates that any LWC that was present was minor and likely limited to the uppermost layer/s. Thus, its volumetric content was not substantial enough to warrant the 8 February 2017 survey being classified as wet snow. We classified the 7 April 2021 survey at Ranch Creek and the 27 May 2021 survey at Cameron Pass as wet snow surveys. Snow temperatures collected in five snow pits at Ranch Creek indicated isothermal conditions with a bulk snowpack temperature of − 0.5 °C and surface melt was noted during GPR collection. Snow temperatures were not collected for the 27 May 2021 Cameron Pass survey, but we classified it as a wet snow survey based on the presence of standing water up to 0.12 m in the snow pit.

A.3 | Snow Density Model Parameters

Empirical models range from simpler equations (e.g., Mizukami & Perica, 2008) that require a time parameter and a snow climate parameter, to more complicated equations (Sexstone & Fassnacht, 2014) that require snow depth, geographic (e.g., elevation or UTM coordinates), and time parameters. The required model inputs are listed in Table S2. Empirical models can be calibrated to specific study domains using nearby weather stations which measure snow water equivalent (SWE) and snow depth (McCreight & Small, 2014; Pistocchi, 2016). We chose to forego calibration for two reasons: (1) many of the regions that would benefit from SWE remote sensing are poorly instrumented and, therefore, not capable of model calibration and, (2) the main source of our calibration would be SNOTEL stations near the study areas, which are located in small forest openings, where snow density tends to be underestimated when compared to the unforested areas where most of our transects were located (Bonner et al., 2022). Empirical models were run for our surveys using inputs from the lidar snow depth rasters, but only using grid cells where relative permittivity and density values were derived.

The Snow Data Assimilation System (SNODAS) provides daily SWE and snow depth estimates, which can be divided to calculate snow density. The data are accessible at the National Snow and Ice Data Center (NSIDC; National Operational Hydrologic Remote Sensing Center, 2004). SNODAS datasets that aligned with our survey dates were accessed and reprojected into the coordinate systems for each field site (Table 1). SNODAS has a much larger pixel size (~1000 m) than the derived snow density rasters (3 m), so the median of all derived densities within each SNODAS pixel was calculated to evaluate the SNODAS density estimates.

The iSnobal model (Marks et al., 1999) is incorporated as the heart of the Automated Water Supply Model (AWSM; Havens et al., 2020). AWSM handles all the data formatting, configuration, downscaling, and interpolation of input meteorological data from numerical weather prediction models via the Spatial Modeling for Resources Framework (SMRF). AWSM requires topographic and vegetation information as well as meteorological data at hourly time steps. A 50 m digital elevation model (DEM) and topographic data were generated for the Cameron Pass study area from the USGS National Elevation Dataset (https://www.usgs.gov/tools/national-map-viewer; accessed 1 April, 2023) and the 2014 USGS LandFire dataset (https://landfire.gov/, accessed on 1 April 2023). Hourly meteorological inputs (2 m air temperature and relative humidity, 10 m U- and V-components of wind, total precipitation, downward shortwave radiation flux, and total cloud cover) were derived from the High-Resolution Rapid Refresh (HRRR) atmospheric model hosted by Amazon Web Services (AWS; https://registry.opendata.aws/noaa-hrrr-pds/) and spatially distributed using the AWSM framework. Initially, iSnobal was simulated using precipitation scaling for 1 October through the final survey week of the water years, and subsequently run a second time using a lidar snow depth raster collected by Quantum Spatial Inc. over Cameron Pass on 19 March 2021 (Adebisi et al., 2022) to rescale the precipitation inputs. Precipitation was further scaled based on a comparison between the Joe Wright SNOTEL measured SWE and SMRF-distributed HRRR precipitation. The Susong et al. (1999) snow precipitation density was chosen for the model runs. Median derived densities were calculated for the 50 m iSnobal grid for comparison.

A.4 | Evaluation of Modeled Densities using In-Situ Densities

We assessed the accuracy of modeled densities using a time-series of snow densities observed at the Joe Wright SNOTEL station and snow pit-measured densities from Grand Mesa and Cameron Pass. The time-series analysis compares empirically modeled density and estimated SWE with SNOTEL density and SWE measured during WY 2020 (Figure S12). We found that the Jonas et al. (2009; J_{09}) and Sexstone & Fassnact (2014; $S\&F_{14}$) models yielded the most accurate densities and SWE at the SNOTEL station, whereas the Sturm et al. (2010; St_{10}) model consistently overestimated density and SWE and the Mizukami & Perica (2008; $M\&P_{08}$) model consistently underestimated density and SWE. SWE estimated from $M\&P_{08}$ was the least affected by short-term fluctuations in snow depth, which was problematic for the three depth-based empirical models (e.g., McCreight & Small, 2014). We then calculated RMSEs for each model using snow pit-measured densities from Grand Mesa (n = 164) and Cameron Pass (n = 12) that correspond with the lidar acquisitions (Table S6). At Grand Mesa, St_{10} yielded the most accurate densities (RMSE = 14 kg m^{-3}), whereas J_{09} yielded the most accurate densities (RMSE = 30 kg m^{-3}) at Cameron Pass. SNODAS performed comparably at both field sites (Grand Mesa RMSE = 52 kg m^{-3}; Cameron Pass RMSE = 44 kg m^{-3}). With the exception of the performance of St_{10} at Grand Mesa, these results corroborate the evaluation of modeled densities which uses the lidar-GPR derived densities as the benchmark (Figure 5).

Any use of trade, firm, or product names is for descriptive purposes only and does not imply endorsement by the U.S. Government.